Bioorganic Chemistry 181 (2026) 110335

Contents lists available at ScienceDirect

Bioorganic Chemistry

journal homepage: www.elsevier.com/locate/bioorg

The discovery of potent and selective N^6-modified adenosine derivatives as effective chemotherapeutic agents to overcome p53-dependent drug resistance in cancer and HPIV-3/AdV5 respiratory tract infections

Elżbieta Speina [a], Katherine Burchiellaro [a,b], Marta Denel-Bobrowska [c], Marta K. Dudek [d], Damian Trzybiński [e], Krzysztof Woźniak [e], Agnieszka B. Olejniczak [c], Adam Mieczkowski [a,*]

[a] Institute of Biochemistry and Biophysics, Polish Academy of Sciences, Pawińskiego 5a, 02-106 Warsaw, Poland
[b] Faculty of Chemistry, University of Warsaw, Pasteura 1, 02-093 Warsaw, Poland
[c] Institute of Medical Biology, Polish Academy of Sciences, 106 Lodowa, 93-232 Łódź, Poland
[d] Centre of Molecular and Macromolecular Studies, Polish Academy of Sciences, Sienkiewicza 112, 90-363 Łódź, Poland
[e] Biological and Chemical Research Centre, Chemistry Department, University of Warsaw, Żwirki i Wigury 101, 02-089 Warsaw, Poland

ARTICLE INFO

Keywords:
N^6-modified adenosine derivatives
Cytotoxicity
Antiviral activity (**HPIV-3**, **AdV5**)
p53
Apoptosis
Fludarabine
Cladribine

ABSTRACT

A library of N^6-modified adenosine derivatives (compounds **7**–**36**) was synthesized *via* a one-step reaction of 6-chloro- or 2-amino-6-chloro-(β-D-ribofuranosyl)-9*H*-purine with primary or secondary amines. The structures of selected compounds (**14**, **31**, **34**) were confirmed by single-crystal X-ray diffraction, revealing diverse crystal packing motifs and hydrogen-bonding networks. Biological evaluation demonstrated a broad range of cytotoxic activities across a panel of cancer and non-cancer cell lines, ranging from highly potent to non-toxic derivatives. Structure–activity relationship analysis revealed that the biological properties of the synthesized compounds were strongly influenced by the nature of the N^6 substituent, with distinct structural features governing anticancer and antiviral activities. Several compounds (**21**, **22**, **28**, **30**, and **32**) markedly reduced cancer cell viability, with compound **28** exhibiting the highest potency across multiple solid tumor models. Importantly, compound **28** induced apoptosis, suppressed proliferation, and rapidly decreased cell viability in both HCT116 and HCT116 p53−/− colorectal carcinoma cells, indicating p53-independent activity. In contrast, cladribine displayed pronounced p53 dependence, promoting apoptosis primarily in p53-proficient cells and inducing a senescence-like phenotype rather than rapid cell death. Antiviral screening identified compounds **22**, **25**, and **35** as promising inhibitors of human parainfluenza virus type 3 (**HPIV-3**), whereas compound **12** exhibited the highest activity and selectivity against human adenovirus type 5 (**AdV5**). Collectively, these findings identify N^6-modified adenosines as a promising class of compounds for developing anticancer agents with p53-independent activity and reveal several derivatives as attractive scaffolds for further optimization toward antiviral agents targeting respiratory viruses.

1. Introduction

Nucleoside analogues represent an important class of biologically active molecules with significant therapeutic potential. They are widely used as antiviral [1,2] and anticancer [3–5] agents due to their unique chemical and biological properties. Among them, adenosine analogues and derivatives have demonstrated promising anticancer potential through diverse mechanisms of action that target multiple cellular pathways and processes. The adenosine analogue, N^6-isopentenyladenosine (Riboprine) (**1**) (Fig. 1), inhibits cancer cell

Abbreviations: **AdV5**, Human adenovirus type 5; CC_{50}, 50% cytotoxic concentration; CL, Cladribine (2-chloro-2′-deoxyadenosine); CPE, Cytopathic effect; DMSO, Dimethyl sulfoxide; FBS, Fetal bovine serum; FL, Fludarabine (2-fluoro-9-β-D-arabinofuranosyladenine); **HCMV**, Human cytomegalovirus; **HPIV-3**, Human parainfluenza virus type 3; **HSV-1**, Human herpes simplex virus type 1; IC_{50}, 50% inhibitory concentration; MTT, 3-(4,5-dimethylthiazol-2-yl)-2,5-diphenyltetrazolium bromide; NMR, Nuclear magnetic resonance; PBS, Phosphate-buffered saline; PI, Propidium iodide; SAR, Structure–activity relationship; SI, Selectivity index; TP53, Tumor protein p53 gene; XRD, X-ray diffraction..

* Corresponding author.
E-mail address: amiecz@ibb.waw.pl (A. Mieczkowski).

https://doi.org/10.1016/j.bioorg.2026.110335
Received 6 February 2026; Received in revised form 30 July 2026; Accepted 3 August 2026
Available online 5 August 2026

proliferation by modulating the activity of farnesyl pyrophosphate synthase (FPPS) [6]. Riboprine significantly suppresses the growth of several human cancer cell lines, including MCF7 (breast adenocarcinoma) [7], J82 (bladder carcinoma) [8], and A375 (melanoma) [9]. Another analogue, Tubercidin (**2**, 7-deazaadenosine), exhibits cytotoxicity against the mouse lymphoma cell line P388 and the human lung carcinoma cell line A549 [10]. Tubercidin (**2**) is incorporated into DNA and inhibits DNA and RNA polymerases, thereby blocking nucleic acid and protein synthesis.

Cladribine (2-chloro-2′-deoxyadenosine, CL) (**3**) and Fludarabine (2-fluoro-9-β-D-arabinofuranosyladenine, FL) (**4**) are clinically used anticancer nucleoside analogues for the treatment of various leukemias. CL is phosphorylated by deoxycytidine kinase (DCK) to form 2-chlorodeoxyadenosine 5′-monophosphate (2-CdAMP), which is further converted into the triphosphate form (2-CdATP). Incorporation of 2-CdATP into DNA leads to the accumulation of DNA damage, inhibition of DNA synthesis, and subsequent DNA fragmentation, ultimately triggering apoptosis [11]. A critical determinant of apoptosis and the cellular response to DNA damage is the tumor suppressor protein p53, which regulates cell cycle arrest, DNA repair, and programmed cell death [12–14]. Many cancers harbor *TP53* mutations, leading to impaired apoptotic responses and resistance to chemotherapy [15–17]. Therefore, the development of nucleoside analogues that induce apoptosis independently of p53 status is of high therapeutic relevance. In addition to apoptosis, cancer cells may respond to chemotherapeutic stress by entering cellular senescence, a stable form of cell-cycle arrest characterized by enlarged cell morphology, altered nuclear architecture, and sustained metabolic activity [18–20]. Therapy-induced senescence has been increasingly recognized as an alternative outcome of anticancer treatment, particularly in response to DNA-damaging agents and nucleoside analogues. While senescence can initially suppress tumor growth, senescent cells often remain viable and metabolically active, and their long-term persistence has been associated with pro-tumorigenic effects, therapy resistance, and disease relapse. Importantly, the induction of senescence *versus* apoptosis may depend on both the genetic background of cancer cells, including *TP53* status, and the specific molecular properties of the therapeutic agent. Consequently, distinguishing between cytotoxic and senescence-associated responses is critical for the development of effective anticancer nucleoside analogues.

Besides its role in nucleic acid metabolism, adenosine also serves as the natural ligand for G protein-coupled P1 receptors, also known as adenosine receptors, which are differentially expressed across tissues. Based on their pharmacological, biochemical, and molecular properties, these receptors are classified into four subtypes: A_1, A_{2A}, A_{2B}, and A_3. Recent studies have demonstrated that antagonizing the A_1 receptor can exert antitumor effects against glioblastomas [21]. Therefore, adenosine analogues may exhibit anticancer activity not only by interfering with DNA synthesis but also by modulating adenosine receptor signaling.

Importantly, N^6-substituted adenosine derivatives constitute a well-established class of nucleoside analogues that have been explored previously in medicinal chemistry. Some representatives of this structural family included in the current study have already been reported in the literature and patents; nevertheless, the anticancer and antiviral activities of these scaffolds, particularly their ability to overcome p53-dependent drug resistance and their activity against respiratory pathogens such as **HPIV-3** and **AdV5**, remain poorly characterized. Therefore, as part of our continuous research on bioactive nucleoside analogues, including cyclonucleosides [22], azidonucleosides [23], bicyclic pyrimidine nucleosides [24,25], and boron-cluster-modified nucleosides [26–28], we designed and synthesized a library of N^6-modified adenosine derivatives (Scheme 1 and Fig. 2). These compounds were evaluated for both anticancer and antiviral in a panel of human cancer and non-cancer cell lines, as well as against four representative viruses, including respiratory tract pathogens (**HPIV-3**, **AdV5**). Several derivatives exhibited pronounced and selective antitumor activity, while a limited subset displayed favorable antiviral activity and/or selectivity, underscoring their potential as leads for further development and for elucidating distinct cellular responses, including cytotoxic and senescence-associated effects.

2. Materials and methods

2.1. Chemistry (synthesis, spectra)

The ^{1}H and ^{13}C NMR spectra were acquired on a Bruker Avance III 500 spectrometer (Bruker BioSpin, Billerica, Massachusetts, USA), operating at the resonance frequencies of 500.13 MHz and 125.75 MHz for ^{1}H and ^{13}C, respectively. The spectrometer was equipped with a 5 mm BBI probe head with an actively shielded *Z*-gradient coil connected to a GAB/2 gradient unit capable of producing B_0 gradients with a maximum strength of 50 G/cm. The temperature was set to 295 K for all experiments and stabilized using a BCU 05 cooling unit controlled by a BVT3200 variable-temperature unit. Spectra were recorded in 5 mm NMR tubes using DMSO-d_6 as the solvent. Chemical shifts were referenced to the residual solvent signals at 2.50 and 39.50 ppm for ^{1}H and ^{13}C, respectively. All experiments were performed using the original Bruker pulse sequences. The spectra were analyzed using the TopSpin 4.3.0 program (Bruker BioSpin).

*General synthesis of compounds **7**–**36**.* One equivalent of 6-chloro-(β-D-ribofuranosyl)-9*H*-purine (**5**) or 2-amino-6-chloro-(β-D-ribofuranosyl)-9*H*-purine (**6**) (typically 4 mmol, 1.15 g of **5** or 1.21 g of **6**) was dissolved in ethanol (30 mL), and 1.5 equivalents of the appropriate primary or secondary amine were added, followed by 3 equivalents of triethylamine. The reaction mixture was refluxed for 18 h and then cooled to room temperature. Evaporation with silica gel, followed by column chromatography using silica gel and 10–20% methanol in chloroform, yielded pure compounds **7**–**36**. All N^6-modified adenosine derivatives in this study were synthesized or resynthesized using our general procedure, purified, and fully characterized by NMR and HRMS,

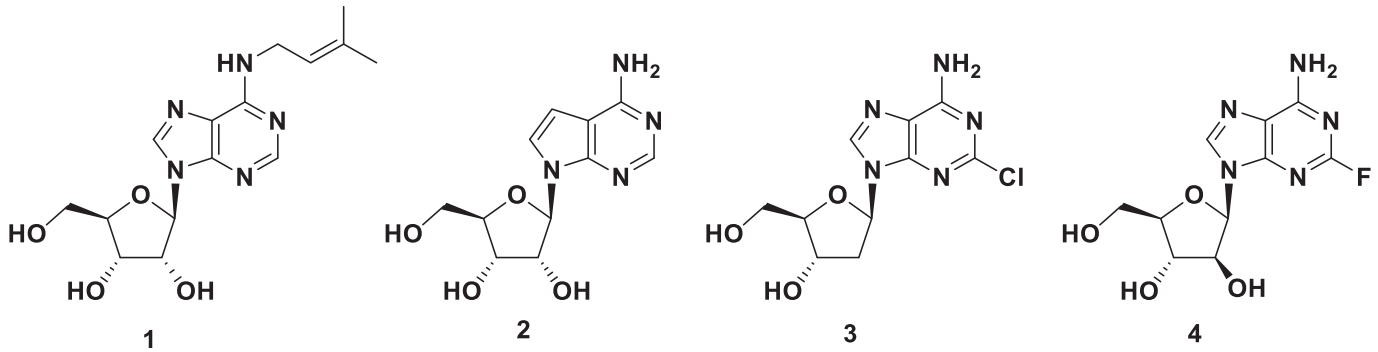

Fig. 1. Examples of Adenosine analogues with anticancer activity: Riboprine (**1**), Tubercidin (**2**), Cladribine (**3**), and Fludarabine (**4**).

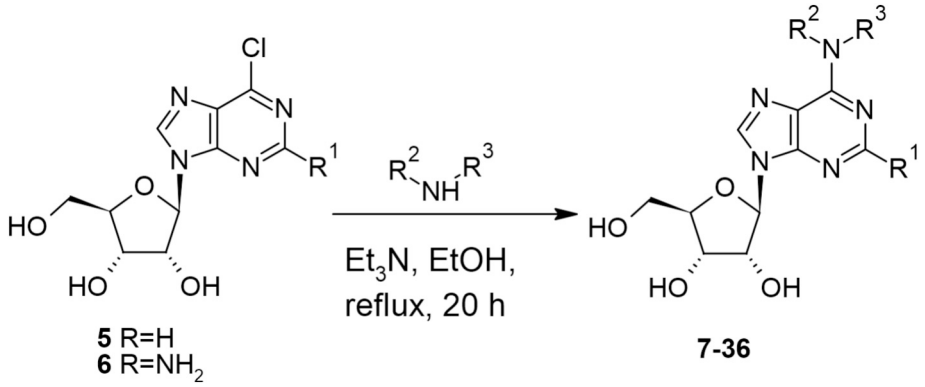

Scheme 1. The general method for the synthesis of N^6-modified adenosine derivatives.

confirming their identity and analytical purity. Analytical data for compounds **7**–**36** and figures of NMR spectra (Figs. S10–S39) are provided in the SI_1 file.

2.2. X-ray crystallography

Good-quality single crystals of **14**, **31**, and **34** were selected for X-ray diffraction experiments at $T = 100$ (2) K. Crystals were mounted with paratone-N oil using the MiTeGen micromounts. Diffraction data were collected on the Agilent Technologies SuperNova Dual Source diffractometer with CuKα radiation ($\lambda = 1.54184$ Å) using CrysAlis Pro software [29]. Empirical multi-scan absorption correction using spherical harmonics (**14** and **31**) and the analytical numeric absorption correction using a multifaceted crystal model based on expressions derived by Clark and Reid (**34**) [30], implemented in the SCALE3 ABSPACK scaling algorithm, were applied [29]. The structural determination procedure was carried out using the SHELX package. The structure was solved by the intrinsic phasing method using SHELXT [31] and subsequent least-squares refinement was performed using the full-matrix least-squares method on F^2 with SHELXL [32]. All H-atoms linked to the N and O-atoms were located on a difference Fourier map and refined with $U_{iso}(H) = xU_{eq}(N,O)$, where x = 1.2 for the amine and 1.5 for the hydroxyl H-atoms, respectively. All O–H bonds were subject to DFIX 0.82 restraints. In the case of **31**, an additional DFIX 0.87 was applied for the N–H bonds. The remaining H-atoms were positioned geometrically, with C—H equal to 0.95, 0.98, 0.99, and 1.00 Å for the aromatic, methylene, methine, and methyl H-atoms, respectively, and constrained to ride on their parent atoms with $U_{iso}(H) = xU_{eq}(C)$, where x = 1.2 for the aromatic, methylene, and methine H-atoms, and x = 1.5 for methyl H-atoms, respectively. The interactions in the crystals of both investigated compounds have been identified using the PLATON program [31]. Figures were prepared using Olex2 and Mercury software [33,34].

2.3. Cytotoxic and antiviral activities

2.3.1. Cytotoxicity assay

The cytotoxic properties of the tested compounds were evaluated in the following cell lines: Vero (*Cercopithecus aethiops* normal kidney epithelial cells); LLCMK2 (*Macaca mulatta* normal kidney epithelial cells), MRC-5 (human normal lung fibroblasts), HeLa (human cervix adenocarcinoma cells), A-431 (human epidermoid carcinoma), A-549 (human lung carcinoma), NCI-H1299 (human p53-deficient lung carcinoma), HCT116 and HCT116 p53−/− (human colorectal carcinoma), and BJ (human epidermoid normal fibroblasts), MRC-5 (human lung normal fibroblasts). The Vero, LLCMK2, HeLa, A-431, A-549, NCI-H1299, HCT116, BJ, and MRC-5 cell lines were purchased from the American Type Culture Collection (ATCC; Manassas, VA, USA). The HCT116 p53−/− cell line was kindly provided by Professor Bert Vogelstein (Johns Hopkins University, Baltimore, MD, USA).

Cells were cultured in either Minimum Essential Medium (MEM; Merck, Sigma-Aldrich, Darmstadt, Germany) or Dulbecco's Modified Eagle Medium (DMEM; Thermo Fisher Scientific, Waltham, MA, USA), both supplemented with 10% fetal bovine serum (FBS; Merck, Sigma-Aldrich), 2 mM L-glutamine, and 1% penicillin/streptomycin solution (10,000 units/mL penicillin G and 10 mg/mL streptomycin; Sigma-Aldrich). Stock solutions of all tested compounds were prepared in dimethyl sulfoxide (DMSO; Merck, Sigma-Aldrich) and diluted in MEM or DMEM supplemented with 10% FBS, 2 mM L-glutamine, and antibiotics.

After reaching 80–90% confluence, cells were harvested with trypsin (Thermo Fisher Scientific) and seeded into 96-well microplates at 2–20 $\times 10^3$ cells per well. Following an overnight incubation at 37 °C in a humidified atmosphere with 5% CO_2, the culture medium was supplemented with freshly prepared solutions of the tested compounds at final concentrations ranging from 0.1 to 1000 μM. Cytotoxicity was assessed using the MTT assay, with all experiments performed in at least triplicate. Treated and untreated control cells were incubated at 37 °C for 48 or 72 h in a humidified atmosphere containing 5% CO_2 [35,36]. After incubation, cells were exposed to 3-(4,5-dimethylthiazol-2-yl)-2,5-diphenyltetrazolium bromide (MTT; Merck, Sigma-Aldrich) for 2 h and subsequently lysed with 100 μL of a solution containing 45% *N*, *N*-dimethylformamide (DMF; Merck, Sigma-Aldrich) and 13% sodium dodecyl sulfate (SDS; Merck, Sigma-Aldrich). Following overnight incubation at 37 °C, absorbance was measured at 570 nm using a scanning multi-well spectrophotometer (PARADIGM Detection Platform; Beckman Coulter, Brea, CA, USA) or a Varioskan Lux microplate spectrophotometer (Thermo Fisher Scientific). The cytotoxic concentration (CC_{50}), defined as the concentration that reduces cell viability by 50% relative to untreated controls, was calculated by nonlinear regression analysis of the dose–log(concentration)–response curves using GraphPad Prism version 9 (GraphPad Software, San Diego, CA, USA).

2.3.2. Antiviral activity assay

Antiviral activity was evaluated against the following viruses: human herpesvirus 1 (HSV-1), human parainfluenza virus type 3 (HPIV-3), human adenovirus 5 (AdV5), and human herpesvirus 5 (HCMV) grown in the following host cells: Vero, LLCMK2, MRC-5, and HeLa. All viruses were purchased from ATCC. Tested compounds were dissolved in DMSO and then diluted in MEM supplemented with 2% heat-inactivated FBS, 2 mM L-glutamine, and 1% penicillin/streptomycin solution (10,000 units/mL penicillin G with 10 mg/mL streptomycin). Host cells were maintained in MEM supplemented with 10% heat-inactivated FBS and antibiotics. Upon reaching 80–90% confluency, cells were harvested with trypsin and seeded into 96-well microplates at a density of 2×10^4 cells per well. After overnight incubation at 37 °C in a humidified atmosphere containing 5% CO_2, the culture medium was removed from the confluent cells grown in 96-well microplates, and cells were inoculated with virus solutions in MEM containing 2% FBS and antibiotics at

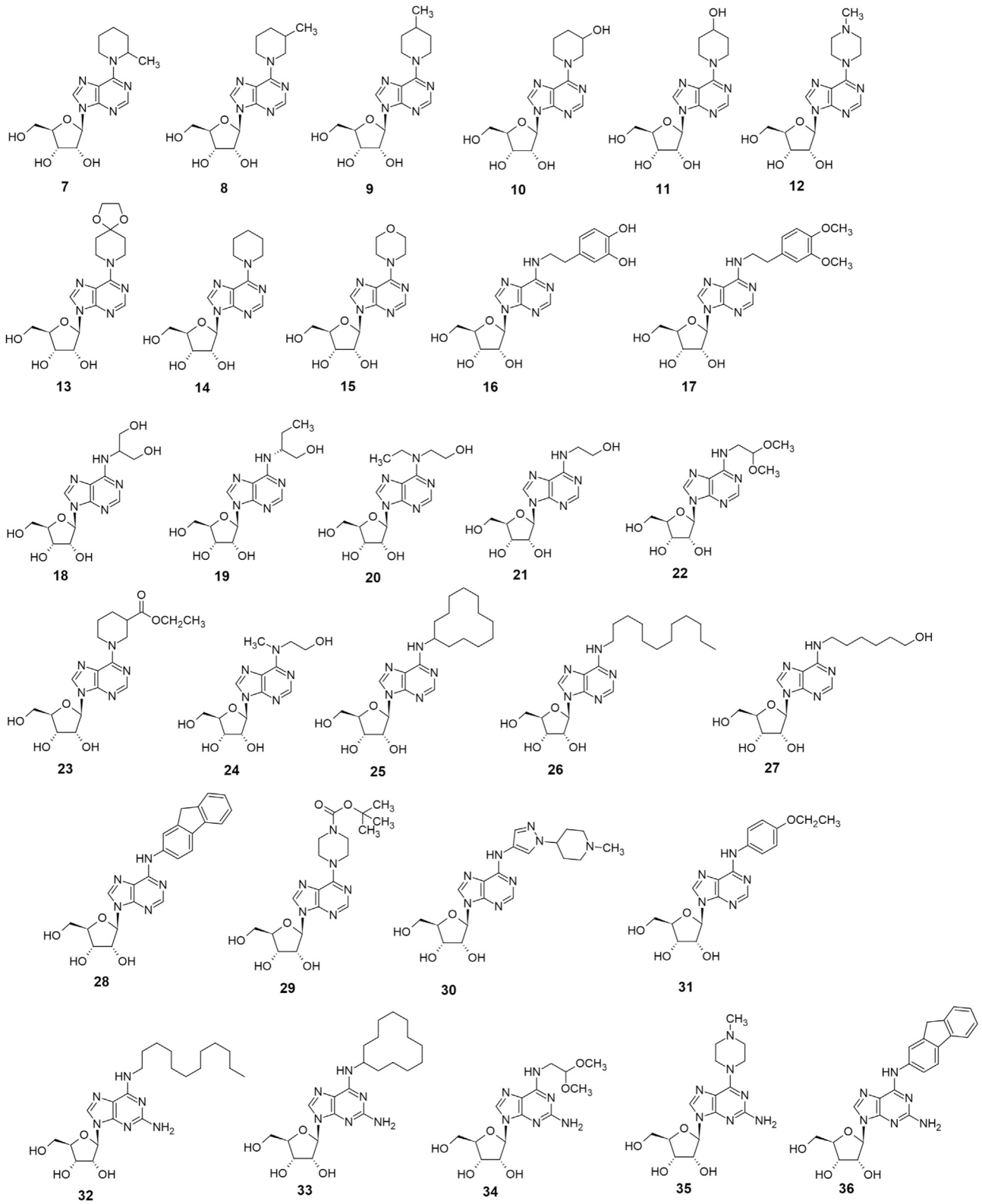

Fig. 2. Structural formulas of N^6-substituted adenosines used in this study.

the following multiplicities of infection (MOI): HSV-1, 0.005; HPIV-3, 0.01; AdV5, 0.005; and HCMV, 20 plaque-forming units per well (PFU)/well. Following virus adsorption for 1 h (HSV-1, HPIV-3, and AdV5) or 2 h (HCMV), residual viral particles were removed. Infected cells were subsequently incubated in MEM supplemented with 2% FBS and antibiotics, along with the tested compounds at concentrations ranging from 0.1 to 1000 μM [35]. All experiments were performed in triplicate. Cell monolayers were incubated with the tested compounds at 37 °C in a humidified atmosphere with 5% CO_2 until a cytopathic effect (CPE) was visible. Viral infection was assessed using the MTT assay (as described above) or, in the case of HCMV, by a plaque-reduction assay. HCMV plaques were counted under an inverted microscope (Olympus

IX73, Olympus, Tokyo, Japan). Antiviral activity was expressed as IC_{50} values, defined as the concentration of the compound required to reduce the number of viral plaques by 50% relative to virus-infected, untreated controls.

2.4. Cell proliferation, cell death, and apoptosis assays

Cell proliferation, cell death, and apoptosis were evaluated using the IncuCyte S3 Live-Cell Imaging System (Sartorius; Essen BioScience, Ann Arbor, MI, USA) in combination with SYTOX™ Green Dead Cell Stain and Annexin V Conjugates for Apoptosis Detection (Thermo Fisher Scientific, cat. no. S34860 and A13203, respectively). Image acquisition and analysis were performed according to the manufacturer's instructions using IncuCyte 2019B Rev2 software (Essen BioScience, https://www.sartorius.com/en/products/live-cell-imaging-analysis/live-cell-analysis-software).

HCT116 and HCT116 p53−/− cells were seeded into 96-well plates at a density of 5×10^3 cells per well 24 h prior to treatment. Four replicates were included for each experimental condition. Cells were treated with compound **28** or CL at final concentrations of 5, 10, or 40 μM and monitored for 96 h, with images acquired every 6 h. For untreated control wells, DMSO was added at the highest concentration used to dissolve compound **28**.

To determine and compare proliferation, cell death, and apoptosis rates, cell numbers were log-transformed and plotted as ln(cell number) *versus* time. The specific growth rate (μ, h^{-1}) was calculated for each replicate as the slope of the linear regression line fitted to the exponential growth phase. Mean μ values from four replicates were compared between HCT116 and HCT116 p53−/− cells using a two-tailed Student's *t*-test. When multiple treatment conditions were analyzed simultaneously, one-way analysis of variance (ANOVA) followed by Tukey's *post hoc* test was used. All statistical analyses were performed using STATISTICA software (version 6). Differences were considered statistically significant at $p < 0.05$.

2.5. Cell cycle analysis

HCT116 and HCT116 p53−/− cells were seeded into 10 cm dishes one day before treatment. Cells were then exposed to compound **28** at a final concentration of 20 μM. At the indicated time points, approximately 1×10^6 cells were harvested, washed with phosphate-buffered saline (PBS), and fixed in cold 70% ethanol overnight at 4 °C. The following day, the samples were centrifuged and resuspended in phosphate-buffered saline (PBS; Merck, Sigma-Aldrich) containing 50 μg/mL propidium iodide (PI; Merck, Sigma-Aldrich) and 50 μg/mL RNase A (Merck, Sigma-Aldrich). DNA content was analyzed using a BD FACSCalibur flow cytometer (BD Biosciences, Franklin Lakes, NJ, USA), with the FL2-A detector set to detect excited PI. Data were acquired using BD CellQuest Pro (BD Biosciences), and results are presented as histograms of nuclear DNA content.

3. Results and discussion

3.1. Synthesis of N^6-modified adenosine derivatives

All new compounds **7**–**36** (Fig. 2) used in this study were synthesized from 6-chloro-(β-D-ribofuranosyl)-9*H*-purine (**5**) or 2-amino-6-chloro-(β-D-ribofuranosyl)-9*H*-purine (**6**) in a one-step reaction with an appropriate primary or secondary amine. The reactions were carried out in boiling ethanol in the presence of triethylamine as a base (Scheme 1). The detailed procedure is described in the Experimental section, while the physicochemical characteristics of all new derivatives are described in the SI_1 file. The structures of the synthesized compounds were confirmed by NMR spectroscopy and HRMS, while single-crystal X-ray diffraction analysis was performed for selected representative derivatives to provide unambiguous structural confirmation of the N^6-substitution pattern and overall molecular architecture.

3.2. Crystal structures of selected compounds

Single-crystal X-ray diffraction analysis confirmed the proposed constitution of three nucleosides −**14**, **31**, and **34**. These compounds crystallize in the monoclinic $P2_1$ (**14** and **34**) and orthorhombic $P2_12_12_1$ (**31**) space groups with one (**14** and **31**) or two molecules (**34**) in the asymmetric unit of the crystal lattice (Fig. 3). The presence of two crystallographically independent molecules in the structure of the compound **34** is related to the noticeably different spatial orientation of the substituent attached to the C4 atom relative to the purine moieties (see Fig. S1, SI_1). The details of crystallographic data and refinement parameters for all investigated compounds are summarized in Table S1 (SI_1). The complete list of bond lengths, valence, and torsion angles is provided in Tables S2–S10 (SI_1).

In all analyzed nucleosides, the ribose ring is attached to the endocyclic N-atom of the purine moiety *via* a glycosylic bond. As for the pentose, the values of Cremer & Pople puckering [37] and Altona-Sundaralingam pseudorotation parameters [38] (Table 1) indicate that the nearest furanose pucker descriptor for this moiety is E(nvelope) C2′-endo for all analyzed compounds. Simultaneously, the values of χ (rotation around glycosylic bond C1′–N1) and γ (rotation around the C4′–C5′ bond) correspond to the +sc (+gauche) arrangement. As for the overall geometry of the nucleosides in analyzed crystals, the conformation with the edge of purine moiety directed toward the pentafuranose ring favors the performance of intramolecular O–H···O hydrogen bond between the hydroxyl at the C5 end of the ribose and the endocyclic N4 atom of the purine six-membered ring (Fig. 1) in all investigated systems (d(D···A) = 2.740 (4), 2.702 (2)/2.794 (2) (molecule A/molecule B) and 2.752 (2) Å; <(D–H···A) = 168 (4), 174 (3)/159 (3) (molecule A/molecule B) and 165 (2)° (values for **14**, **34** and **31**, respectively (Fig. 1; Tables S12, S14 and S16, SI_1). In the case of **14,** also a weak intramolecular C–H···N hydrogen bond engaging one of the methylene H-atoms of the substituent and the N2 atom of the five-membered ring of the purine (d(D···A) = 3.008 (4) Å; <(D–H···A) = 140°; Table S12, SI_1).

Investigated compounds are substituted with different functional groups of various sizes and constitutions, which is also reflected in the appearance of their crystal networks. A close look at the drawing of the packing of individual nucleosides reveals differences among them (Fig. 4).

Thus, the **14** forms a characteristic "*herring-bone*" arrangement, in which the molecules in the crystal are ordered into infinite layers running along the (001) plane (Fig. 4A). The molecules within such formed layers are connected through the network of the O–H···O hydrogen bonds (Table S12, SI_1) and weak C–H···π interactions (Table S11, SI_1). The entire structure is additionally stabilized by the network of weak C–H···π contacts involving some methylene H-atoms of the substituent and aromatic purine rings of neighboring molecules in adjacent layers (Table S11, SI_1). The layers can also be distinguished when it comes to the crystal structure of **34**. However, they have a bilayered structure and spread along different planes (namely, (010)) (Fig. 4B). A single bilayer is composed of A and B molecules of the compound interacting with themselves *via* a dense network of hydrogen bonds of various types (O–H···O, O–H···N, N–H···O, and C–H···O) (Table S14, SI_1). Additionally, neighboring molecules creating the bilayer are oriented to themselves in a way that results in the appearance of the π-π contacts (Table S13, SI_1) between the six-membered rings of their purine moieties (the distance between the geometric centers of gravity of these rings is 3.3434 (8) Å). The entire crystal network is stabilized by weak C–H···O contacts that engage adjacent molecules from neighboring bilayers (Table S14, SI_1). Adjacent bilayers are parallel to each other, but due to the existence of the two-fold screw axis, they are rotated 180° relative to each other. The crystal structure of the latter compound (**31**) looks even different (Fig. 4C). In this case,

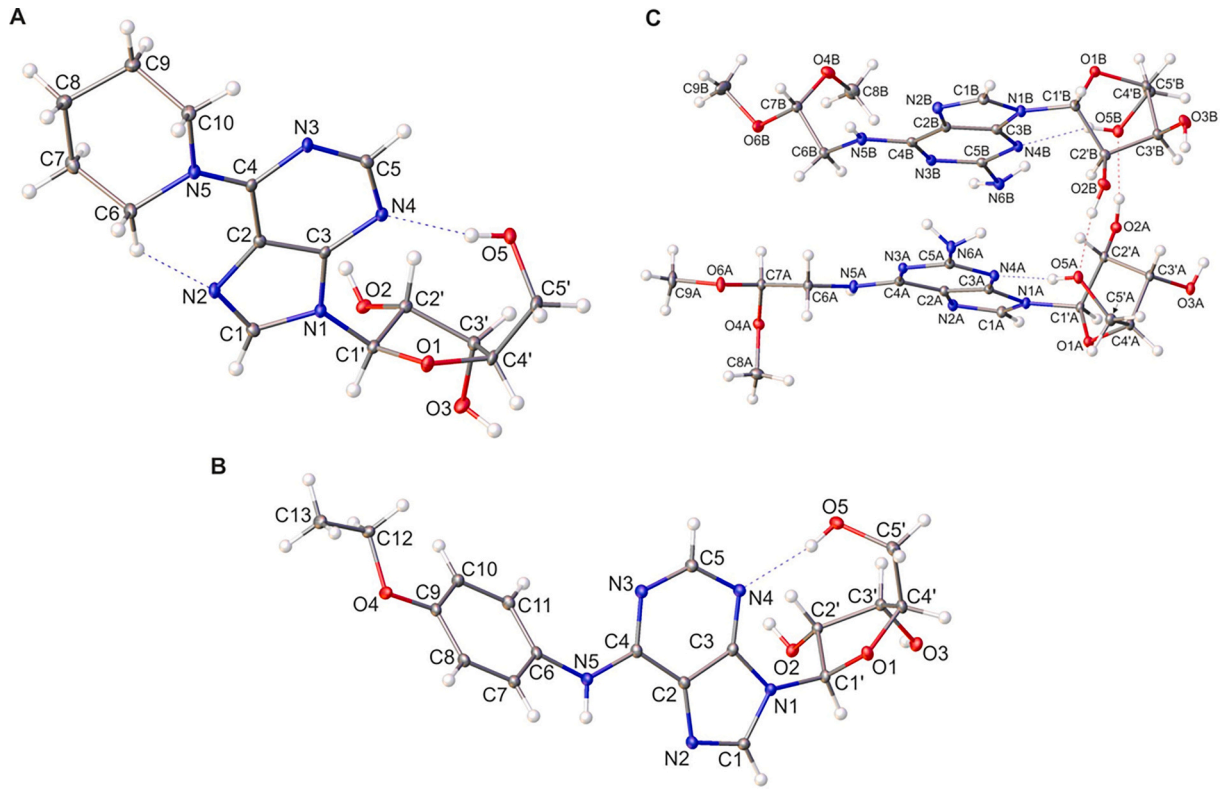

Fig. 3. The asymmetric unit of the crystal lattice of **14** (a), **31** (b), and **34** (c) with crystallographic atom numbering. Displacement ellipsoids are drawn at the 50% probability level, and H atoms are shown as small spheres of arbitrary radius. Dashed lines represent the hydrogen bonds.

Table 1
Cremer-Pople (Φ,q) and Altona-Sundaralingam (P, τ) pseudorotation parameters calculated for the pentafuranose rings within molecules of the investigated compounds, and values of torsion angles for χ (O1–C1′–N1–C3) and γ (C3′–C4′–C5′–O5).

	Compound		
Parameter	14	31	34 (mol. A / mol. B)
Φ [°]	81.8(5)	78.6(2)	77.8(3) / 70.1(3)
q(2) [Å]	0.395(4)	0.3925(18)	0.348(2) / 0.351(2)
P [°]	170.6(3)	167.1(2)	165.9(2) / 157.9(2)
τ [°]	40.4(2)	40.2(1)	35.7(1) / 36.4(1)
χ [°]	54.7(4)	67.1(2)	58.5(3) / 61.5(3)
γ [°]	51.1(4)	45.4(2)	46.1(3) / 54.9(2)

molecules are held together by the network of O–H···N and N–H···O hydrogen bonds (Table S16, SI_1) in infinite chains running along the [001] direction. Each chain is additionally stabilized by the weak C–H···π contacts (Table S15, SI_1), engaging the aromatic H-atom of the five-membered ring of the purine moiety and the six-membered ring of the substituent of adjacent molecules within the chain. In the next step, adjacent chains interact with each other *via* the complex network of the O–H···O and the C–H···O hydrogen bonds and the weak C–H···π contacts (Tables S15 and S16, SI_1).

When it comes to the degree of filling the space in the crystal, the compounds do not differ much from each other. Thus, their structures occupy 67.82, 68.20, and 65.94% for **14**, **31**, and **34**, respectively.

3.3. Cytotoxic and antiviral activity

The cytotoxic properties of the synthesized compounds were evaluated in a panel of human cancer cell lines, including A-431 (epidermoid carcinoma), A-549 (lung carcinoma), NCI-H1299 (p53-deficient lung carcinoma), and HCT116 (colorectal carcinoma), as well as their isogenic p53-knockout counterpart (HCT116 p53−/−). Two non-cancerous fibroblast cell lines were used as controls: BJ (human epidermoid fibroblasts) and MRC-5 (human lung fibroblasts). Cell viability was assessed using the MTT assay, and results were expressed as CC_{50} values (50% cytotoxic concentration). Fludarabine (FL), cladribine (CL), and cisplatin were used as clinically relevant reference anticancer agents. Although these drugs are not direct structural analogues of the synthesized N^6-modified adenosine derivatives, they were selected to provide pharmacologically meaningful benchmarks for comparison, as FL and CL are clinically established purine nucleoside analogues, while cisplatin remains a standard chemotherapeutic agent used in solid tumor treatment. The results are summarized in Tables 2–5, Fig. 5, and Figs. S2–S4 (SI_1). Overall, the tested derivatives displayed a broad range of cytotoxic activities across the cell panel, from highly active compounds ($CC_{50} < 1$ μM) to derivatives showing no detectable toxicity up to 500 μM. In A-431 and BJ cell lines (skin cancer *vs.* normal fibroblasts), the strongest cytotoxic effects toward A-431 cells were observed for compounds **28** and **30** ($CC_{50} = 3.71 \pm 0.82$ μM and 2.22 ± 0.98 μM, respectively). However, due to their concomitant toxicity against BJ fibroblasts ($CC_{50} = 11.58 \pm 3.84$ μM and 11.61 ± 8.46 μM, respectively), the resulting selectivity indexes (SI) were relatively low (SI = 3.12 and 5.23, respectively; Table 2). The highest selectivity toward the A-431 cancer cell line was observed for compounds **21** and **22**, with SI values >8.71 and > 6.68, respectively, accompanied by favorable cytotoxic activity ($CC_{50} = 18.36 \pm 1.27$ μM and 23.96 ± 2.69 μM, respectively). Notably, the clinically used reference drugs FL and CL, although primarily used in hematological malignancies, showed remarkably high selectivity for the solid tumor-derived A-431 cell line (SI > 37.65 and SI > 500, respectively; Table 2). In the lung cancer cell line A-549, the most pronounced cytotoxic effects were observed for compounds **26**, **28**, and **32** ($CC_{50} = 9.5 \pm 5.09$ μM, 9.21 ± 1.85 μM, and 10.93 ± 6.49 μM, respectively). A similar trend was observed in the p53-deficient lung cancer cell line NCI-H1299, where the same derivatives showed CC_{50} values of 9.86 ± 1.15 μM, 10.36 ± 1.24 μM, and $9.08 \pm$

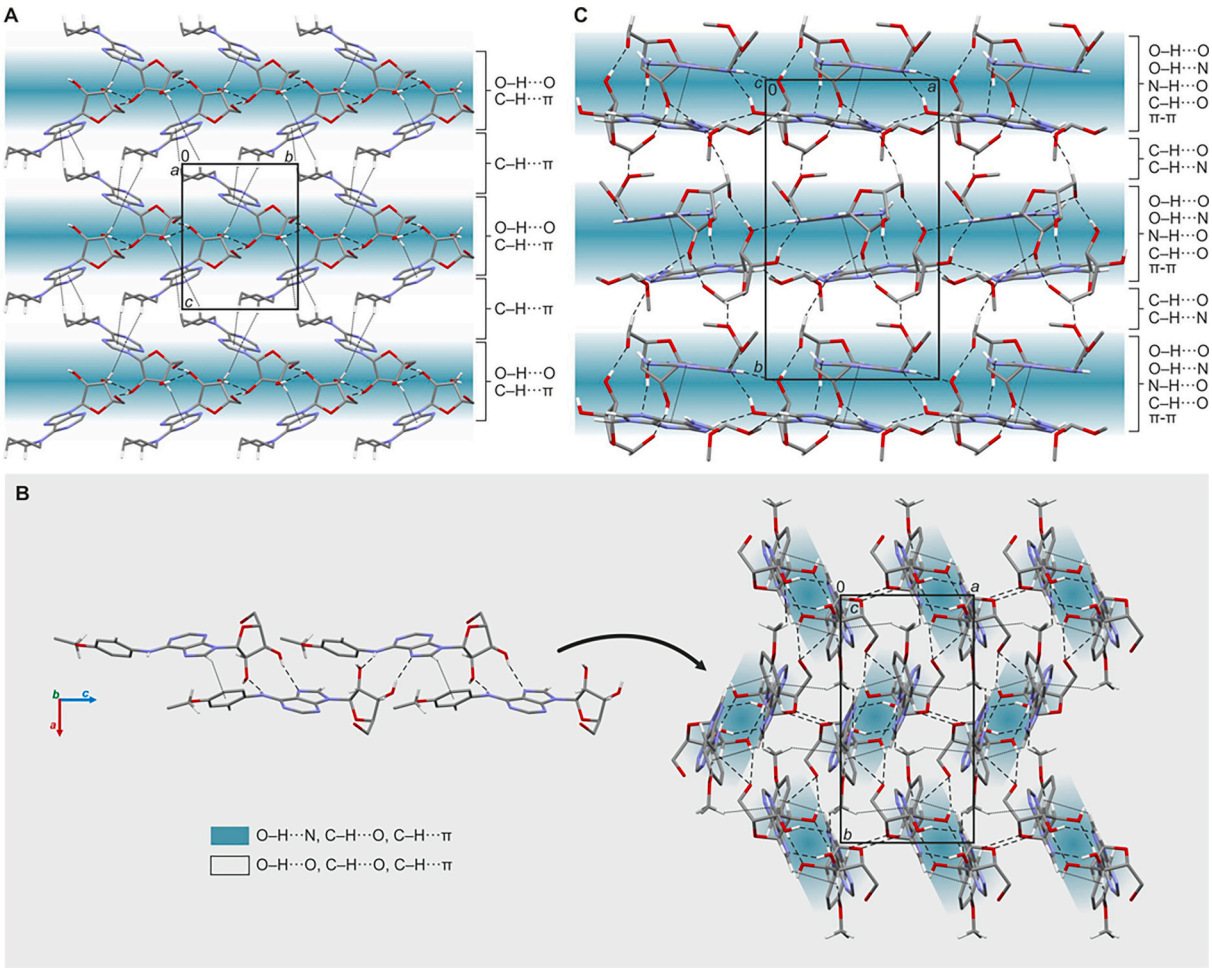

Fig. 4. Supramolecular architecture of **14** (a), **31** (b), and **34** (c) in their crystals. Characteristic structural entities (layers in **14**, bilayers in **34,** and infinite chains in **31**) are highlighted in blue. Hydrogen bonds are represented by dashed lines, where C–H···π are represented by dotted lines. The H atoms not participating in the intermolecular interactions are omitted for clarity. (For interpretation of the references to colour in this figure legend, the reader is referred to the web version of this article.)

5.17 μM, respectively. However, the SIs obtained for both lung cancer models were moderate to low, with the highest values observed for compounds **26** (SI = 6.09 for A-549 and SI = 5.86 for NCI-H1299) and **32** (SI = 4.23 for A-549 and SI = 5.09 for NCI-H1299). Interestingly, A-549 cells, but not the NCI-H1299 cells, were highly sensitive to cladribine, an effect not observed for fludarabine or cisplatin (Table 3).

The ability to evade growth inhibition is a hallmark of cancer cells, enabling them to sustain continuous proliferative signaling. Multiple genes encode tumor suppressor proteins, including *TP53*, which restrict cell growth through several mechanisms [39,40]. To determine whether the observed cytotoxic effect of our newly synthesized adenosine derivatives depends on the p53 protein, a key factor in tumor drug resistance, we performed MTT assays for selected adenosine derivatives (**25**, **26**, **28**, **30**, **32**, **33,** and **36**) using p53-proficient HCT116 cells and in the isogenic p53-null HCT116 p53−/− cell line. Cell viability profiles and calculated CC_{50} values are presented in Fig. 5, Figs. S2–S4 (SI_1), and Table 4. HCT116 p53−/− cells exhibited a 7.93 ± 1.78-fold greater resistance to FL compared to HCT116 cells (CC_{50} = 41.15 ± 12.18 μM *vs.* 5.12 ± 0.69 μM; $p = 0.0095$). For CL, CC_{50} values were 0.56 ± 0.16 μM (HCT116 p53−/−) and < 0.32 μM (HCT116; $p = 0.0072$), while for cisplatin, they were 10.5 ± 2.41 μM and 3.97 ± 0.92 μM, respectively ($p < 0.001$). These findings are consistent with the higher sensitivity of p53-proficient cells to FL and CL. In contrast, the cytotoxic effects of compounds **25**, **26**, **28**, **30**, **32**, **33**, and **36** were independent or less dependent on p53 status, with SI values ranging from 1.15 to 2.31 ($p > 0.05$).

For the evaluation of antiviral activity, four cell lines were used as hosts for viral replication: Vero (*Cercopithecus aethiops* normal kidney cells), LLCMK2 (*Macaca mulatta* normal kidney cells), MRC-5 (human lung normal fibroblasts), and HeLa (human cervix adenocarcinoma cells). The synthesized compounds were screened against four DNA viruses—human herpesvirus 1 (**HSV-1**) and human herpesvirus 5 (**HCMV**), both members of the *Herpesviridae* family, and human adenovirus 5 (**AdV5**, *Adenoviridae* family)—and one RNA virus, human parainfluenza virus type 3 (**HPIV-3**, *Paramyxoviridae* family). Antiviral activity was expressed as IC_{50} (50% inhibitory concentration) and is summarized in Table 5. For compounds with antiviral activity, the SI was calculated. This SI is defined as the ratio of a compound's toxic concentration (CC_{50}) to its effective bioactive concentration (IC_{50}). It is important to note that the SI assessment is relative, and no universally accepted minimum SI threshold has been established [37]. The results demonstrated that compounds **22**, **25**, and **35** were the most effective antivirals against **HPIV-3**, with IC_{50} values of 3.12 ± 0.38 μM, 1.80 ± 0.35 μM, and 23.75 ± 0.35 μM, respectively. Compounds **35** and **22** exhibited the highest observed SI values of ≥42.11 and 16.26, respectively, making them promising candidates for further structure-activity optimization. Unfortunately, the most potent antiviral effect observed for **25** was accompanied by notable cytotoxicity toward host cells (SI = 1.93). Against **AdV5**, the best antiviral activity and selectivity were observed for compound **12**, bearing an *N*-methylpiperazine group at C6.

Table 2
Cytotoxicity and selectivity index of selected compounds in human A-431 and BJ cell lines.

	CC_{50} (μM)*			
Compound	A-431	BJ	p[b]	SI
21	18.36 ± 1.27	> 160 (389.23 ± 171.24)[a]	*0.0227*	> 8.71 (19.01)[a]
22	23.96 ± 2.69	> 160 (604.13 ± 406.37)[a]	*0.029*	> 6.68 (34.8)[a]
25	21.33 ± 4.17	61.57 ± 12.47	< *0.001*	2.89
26	12.67 ± 2	65.81 ± 31.47	*0.0042*	5.19
28	3.71 ± 0.82	11.58 ± 3.84	*0.0236*	3.12
30	2.22 ± 0.98	11.61 ± 8.46	0.1928	5.23
32	6.65 ± 1.03	50.73 ± 14.6	*0.0089*	7.63
33	8.23 ± 4.81	18.72 ± 8.67	*0.0199*	2.27
36	8.36 ± 1.76	17.35 ± 5.57	*0.0427*	2.08
Fludarabine	4.25 ± 0.18	> 160	0.0999	> 37.65
Cladribine	< 0.32	> 160	0.2505	> 500
Cisplatin	1.45 ± 0.29	7.25 ± 2.59	< *0.001*	5.00

* Data are presented as mean ± SD. CC_{50} (50% cytotoxic concentration) is defined as the concentration that reduces cell viability by 50% relative to untreated controls.

[a] Values were obtained from nonlinear regression analysis of dose–log(concentration)–response curves.

[b] *p*-values indicate comparisons of CC_{50} values between A-431 and BJ cell lines. Statistical analysis was performed using a two-tailed Student's *t*-test ($p < 0.05$ was considered statistically significant; italicized values indicate statistically significant differences). The selectivity index (SI) was calculated as the ratio of CC_{50} in BJ cells to that in A-431 cells.

Its relatively strong antiviral effect ($IC_{50} = 6.00 \pm 1.00$ μM), combined with good selectivity (SI = 9.95), makes compound **12** a promising scaffold for further optimization toward more potent and selective antiviral agents. Additionally, compound **16** exhibited weak antiviral activity against **AdV5**, with an IC_{50} of 75.00 ± 2.65 μM and a SI of 13.24. For the remaining compounds, antiviral effects against both DNA and RNA viruses were either absent or very weak (SI < 10) within the non-toxic concentration range.

In summary, the synthesized adenosine derivatives exhibited a wide spectrum of cytotoxic activities across multiple human cancer cell lines, ranging from highly potent compounds to derivatives with minimal or no detectable toxicity. Several compounds displayed pronounced antiproliferative effects in solid tumor–derived cell lines, with compound **28** emerging as one of the most active derivatives across epidermoid, lung, and colorectal carcinoma models. Importantly, the cytotoxic effects of selected derivatives, including **28**, were largely independent of p53 status, in contrast to the reference drugs fludarabine and cladribine, whose activity was significantly reduced in p53-deficient cells. Antiviral screening revealed that, for most derivatives, the observed inhibitory effects occurred at concentrations close to host-cell cytotoxicity, limiting their therapeutic relevance. Only compounds **9**, **12**, **16**, **22**, **23**, and **35** displayed clearly favorable selectivity indexes, indicating a meaningful degree of antiviral selectivity (Table 5). Among these, compounds **22** and **35** showed the most pronounced activity against **HPIV-3**, while compound **12** exhibited selective inhibition of **AdV5** replication. Overall, these findings identified distinct subsets of adenosine derivatives with either p53-independent cytotoxic activity or selective antiviral potential, providing a foundation for further structure–activity relationship optimization toward anticancer and antiviral applications. Based on these data, a structure–activity relationship analysis (SAR) was performed and is discussed below.

Table 3
Cytotoxicity and selectivity index of selected compounds in human A-549, NCI-H1299, and MRC-5 cell lines.

	CC_{50} (μM)*				
Compound	A-549	NCI-H1299	MRC-5	*p*	SI
25	19.72 ± 4.08	15.88 ± 5.22	57.78 ± 4.34	*<0.001*[a] *<0.001*[b]	2.93[c] 3.64[d]
26	9.5 ± 5.09	9.86 ± 1.15	57.81 ± 29.94	*0.005*[a] *0.0054*[b]	6.09[c] 5.86[d]
28	9.21 ± 1.85	10.36 ± 1.24	10.79 ± 1.09	0.204[a] 0.6275[b]	1.17[c] 1.04[d]
30	17.46 ± 5.89	32.72 ± 7.06	29.43 ± 4.38	*0.0194*[a] 0.4639[b]	1.69[c] 0.90[d]
32	10.93 ± 6.49	9.08 ± 5.17	46.2 ± 13.12	*0.008*[a] *0.0079*[b]	4.23[c] 5.09[d]
33	10.42 ± 3.86	15.04 ± 6.35	15.84 ± 4.63	*0.0355*[a] 0.7936[b]	1.52[c] 1.05[d]
36	29.04 ± 13.62	158.97 ± 104.1	44.49 ± 14.41	0.1702[a] 0.1142[b]	1.53[c] 0.28[d]
Fludarabine	15.41 ± 2.26	55.72 ± 5.14	24.25 ± 13.53	0.2836[a] *0.0132*[b]	1.57[c] 0.44[d]
Cladribine	< 0.32	5.37 ± 3.12	5.66 ± 4.77	0.1077[a] 0.9232[b]	> 17.69[c] 1.05[d]
Cisplatin	4.99 ± 0.94	6.3 ± 1.56	3.3 ± 0.99	*0.0067*[a] *0.0015*[b]	0.66[c] 0.52[d]

* Data are presented as mean ± SD. CC_{50} (50% cytotoxic concentration) is defined as the concentration that reduces cell viability by 50% relative to untreated controls.

[a] p-values and SI-values indicate comparisons of CC50 values between A-549 and MRC-5 cell lines. Statistical analysis was performed using a two-tailed Student's *t*-test ($p < 0.05$ was considered statistically significant; italicized values indicate a statistically significant difference).

[b] *p*-values and SI-values indicate comparisons of CC_{50} values between NCI-H1299 and MRC-5 cell lines, respectively. Statistical analysis was performed using a two-tailed Student's *t*-test ($p < 0.05$ was considered statistically significant; italicized values indicate a statistically significant difference).

[c] The selectivity index (SI) was calculated as the ratio of CC_{50} in MRC-5 cells to that in A-549 cells.

[d] The selectivity index (SI) was calculated as the ratio of CC_{50} in MRC-5 cells to that in NCI-H1299 cells.

Table 4
Cytotoxicity and selectivity index of selected compounds in human HCT116 and HCT116 p53−/− cell lines.

	CC_{50} (μM)*			
Compound	HCT116	HCT116 p53−/−	p[a]	SI
25	15.21 ± 4.97	17.43 ± 7.79	0.3975	1.15
26	13.12 ± 4.73	17.31 ± 9.14	0.1589	1.32
28	8.8 ± 4.27	10.22 ± 3.79	0.444	1.16
30	13.73 ± 1.34	15.66 ± 2.12	0.1845	1.14
32	12.78 ± 3.65	15.38 ± 4.69	0.1851	1.20
33	13.65 ± 8.09	17.92 ± 7.58	0.1779	1.31
36	22.77 ± 12.47	52.53 ± 46.42	0.1174	2.31
Fludarabine	5.12 ± 0.69	41.15 ± 12.18	*0.0095*	8.04
Cladribine	0.03 ± 0.01	0.56 ± 0.16	*0.0072*	18.67
Cisplatin	3.97 ± 0.92	10.5 ± 2.41	*< 0.001*	2.64

* Data are presented as mean ± SD. CC_{50} (50% cytotoxic concentration) is defined as the concentration that reduces cell viability by 50% relative to untreated controls.

[a] *p*-values indicate comparisons of CC_{50} values between HCT116 and HCT116 p53−/− cell lines. Statistical analysis was performed using a two-tailed Student's *t*-test ($p < 0.05$ was considered statistically significant; italics indicate a statistically significant difference). The selectivity index (SI) was calculated as the ratio of CC_{50} in HCT116 cells to that in HCT116 p53−/− cells.

3.4. Structure–activity relationship analysis

Analysis of the biological data revealed several clear structure–activity relationships among the synthesized N^6-modified adenosine

Table 5
Cytotoxicity in host cells, antiviral activity, and the selectivity index of the compounds studied.

	CC_{50} (μM)*				IC_{50} (μM)*				SI[a]
Compound	HeLa	Vero	LLCMK2	MRC-5	AdV5	HSV-1	HPIV-3	HCMV	
7	65.50 ± 2.50	161.67 ± 10.41	35.33 ± 5.67	75.33 ± 9.86	>65.50	>161.67	>35.33	>75.33	ND[b]
8	64.77 ± 6.43	55.00 ± 2.50	47.67 ± 5.51	20.00 ± 6.00	>64.78	>55.00	>47.67	>20.00	ND[b]
9	545.00 ± 5.00	326.67 ± 10.41	411.667 ± 7.64	260.00 ± 10.00	455.00 ± 5.00	>326.67	47.33 ± 4.62	>260.00	**8.70 (HPIV-3)** 1.20 (AdV5)
10	254.17 ± 6.29	426.83 ± 10.13	363.33 ± 5.77	245.00 ± 10.00	>254.17	>426.83	170.00 ± 17.32	>245.00	2.14 (HPIV-3)
11	82.67 ± 9.87	72.33 ± 0.58	56.50 ± 5.90	62.67 ± 1.16	75.67 ± 8.51	>72.33	>56.50	>62.67	1.09 (AdV5)
12	59.67 ± 2.88	64.67 ± 1.16	10.00 ± 2.00	147.00 ± 4.36	6.00 ± 1.00	>64.67	>10.00	>147.00	**9.95 (AdV5)**
13	0.24 ± 0.01	1.17 ± 0.29	1.15 ± 0.26	58.17 ± 1.61	>0.24	>1.17	>1.15	>58.17	ND[b]
14	56.00 ± 2.00	57.67 ± 6.430	8.00 ± 1.73	25.50 ± 2.78	>56.00	>57.67	>8.00	>25.50	ND[b]
15	313.33 ± 5.77	77.00 ± 1.00	88.67 ± 1.16	198.00 ± 7.21	67.00 ± 5.12	>77.00	>88.67	>198.00	4.67 (AdV5)
16	993.33 ± 11.56	53.33 ± 3.06	358.33 ± 12.58	935.00 ± 13.23	75.00 ± 2.65	>53.33	242.33 ± 2.08	>935.00	1.48 (HPIV-3) **13.24 (AdV5)**
17	67.00 ± 1.73	51.83 ± 6.79	0.88 ± 0.03	237.67 ± 8.74	51.33 ± 2.31	>51.83	> 0.88	>237.667	1.31 (AdV5)
18	312.50 ± 6.61	73.00 ± 1.00	2.67 ± 0.21	246.67 ± 10.067	184.00 ± 12.17	>73.00	>2.67	>246.67	1.70 (AdV5)
19	206.67 ± 5.77	92.00 ± 6.93	0.08 ± 0.01	>1000	>206.67	>92.00	>0.09	>1000	ND[b]
20	426.67 ± 15.28	390.00 ± 10.00	74.00 ± 5.29	>1000	315.00 ± 17.32	>390.00	>74.00	>1000	1.35 (AdV5)
21	266.67 ± 12.20	277.33 ± 15.14	0.51 ± 0.03	753.33 ± 30.55	123.33 ± 7.57	>277.33	>0.51	>753.33	2.16 (AdV5)
22	272.00 ± 3.46	342.00 ± 13.12	50.67 ± 9.24	698.33 ± 17.56	160.67 ± 12.70	>342.00	3.12 ± 0.38	>698.33	**16.26 (HPIV-3)** 1.69 (AdV5)
23	833.33 ± 23.09	516.667 ± 5.77	533.33 ± 7.64	>1000	>833.333	>516.67	72.50 ± 6.36	>1000	**7.36 (HPIV-3)**
24	>1000	>1000	991.67 ± 14.43	>1000	>1000	>1000	576.67 ± 20.82	>1000	1.72 (HPIV-3)
25	26.00 ± 2.00	20.00 ± 4.00	3.47 ± 0.15	71.67 ± 0.58	>26.000	>20.00	1.80 ± 0.35	>71.66	1.93 (HPIV-3)
26	28.33 ± 1.53	25.00 ± 1.00	6.67 ± 1.16	>1000	>28.333	>25.00	>6.67	>1000	ND[b]
27	0.03 ± 0.01	72.00 ± 15.80	10.67 ± 1.16	>1000	>0.027	>72.00	>10.67	>1000	ND
28	16.33 ± 1.53	20.17 ± 2.75	1.00 ± 0.20	28.67 ± 3.51	>16.33	>20.17	>1.00	>28.67	ND
29	0.02 ± 0.001	0.02 ± 0.003	0.45 ± 0.05	83.33 ± 5.77	>0.02	>0.02	>0.45	>83.33	ND
30	0.68 ± 0.14	40.00 ± 3.54	0.18 ± 0.03	90.67 ± 13.58	>0.68	>40.00	>0.18	>90.67	ND
31	0.02 ± 0.001	4.93 ± 0.83	0.03 ± 0.01	311.67 ± 18.09	>0.02	>4.93	>0.03	>311.67	ND
32	27.33 ± 1.16	20.67 ± 4.16	6.30 ± 1.14	60.00 ± 2.00	>27.333	>20.67	>6.30	>60.00	ND[b]
33	18.00 ± 4.00	6.00 ± 1.00	2.83 ± 0.76	30.00 ± 1.00	>18.000	>6.00	>2.83	>30.00	ND[b]
34	943.33 ± 55.08	>1000	182.50 ± 24.75	>1000	>943.33	>1000	>182.50	>1000	ND
35	576.67 ± 20.82	675.00 ± 13.92	>1000	>1000	>576.67	>675.00	23.75 ± 0.35	>1000	≥ **42.11 (HPIV-3)**
Fludarabine	>1000	520.67 ± 14.58	>1000	>1000	>1000	>520.67	>1000	>1000	ND
Cladribine	665.00 ± 49.50	38.83 ± 9.22	23.33 ± 2.89	933.33 ± 101.93	30.00 ± 5.29	>38.83	>23.33	>933.33	22.17 (AdV5)
Cisplatin	398.00 ± 19.80	0.23 ± 0.03	0.02 ± 0.001	185.67 ± 34.00	42.50 ± 10.6	>0.23	>0.02	>185.67	9.36 (AdV5)

* Data are presented as mean ± SD. CC_{50} denotes the concentration that reduces cell viability by 50% relative to untreated controls.
[a] The selectivity index (SI) was calculated as the ratio of CC_{50} to IC_{50}.
[b] ND, not determined. Bolded SI values indicate compounds displaying relatively favorable antiviral selectivity (SI ≥ 7).

derivatives. Overall, both cytotoxic and antiviral activities were strongly influenced by the nature of the N^6 substituent, particularly its size, polarity, and degree of conformational flexibility (Fig. 2).

3.4.1. SAR for cytotoxic activity

Compounds bearing medium-sized, hydrophobic, or moderately polar N^6 substituents generally exhibited the highest cytotoxic potency across solid tumor–derived cell lines. In particular, derivatives **26**, **28**, **30**, and **32** consistently exhibited low-micromolar CC_{50} values in A-431, A-549, NCI-H1299, and HCT116 cells. Among these, compound **28** exhibited the most pronounced and reproducible cytotoxic activity, suggesting that its N^6 substitution provides an optimal balance between potency and cellular accessibility. Importantly, most active derivatives exhibited comparable cytotoxicity in p53-proficient and p53-deficient HCT116 cells, indicating that N^6 substitution can confer p53-independent anticancer activity, a feature most pronounced for compound **28**. In contrast, derivatives bearing bulkier (**25**,**33**) or highly polar (**36**) substituents generally showed reduced activity or lower selectivity.

A comparison of the most active derivatives suggests that optimal cytotoxic activity requires an N^6 substituent providing a balance between steric bulk, lipophilicity, and conformational adaptability. Compounds bearing medium-sized hydrophobic or moderately polar substituents (*e.g.*, **26**, **28**, **30**, and **32**) consistently exhibited the strongest cytotoxic effects across multiple cancer cell lines, suggesting that these structural features may favor efficient cellular uptake and/or productive interaction with intracellular molecular targets. In contrast, highly bulky or excessively polar substituents generally reduced cytotoxic potency, likely due to steric constraints or impaired membrane permeability.

3.4.2. SAR for selectivity toward cancer versus normal cells

Selectivity for cancer *versus* normal cells was favored among compounds with moderate cytotoxic potency and reduced toxicity toward fibroblasts, as exemplified by compounds **21** and **22** in the A-431/BJ model. In contrast, highly potent derivatives such as **28** and **30** exhibited

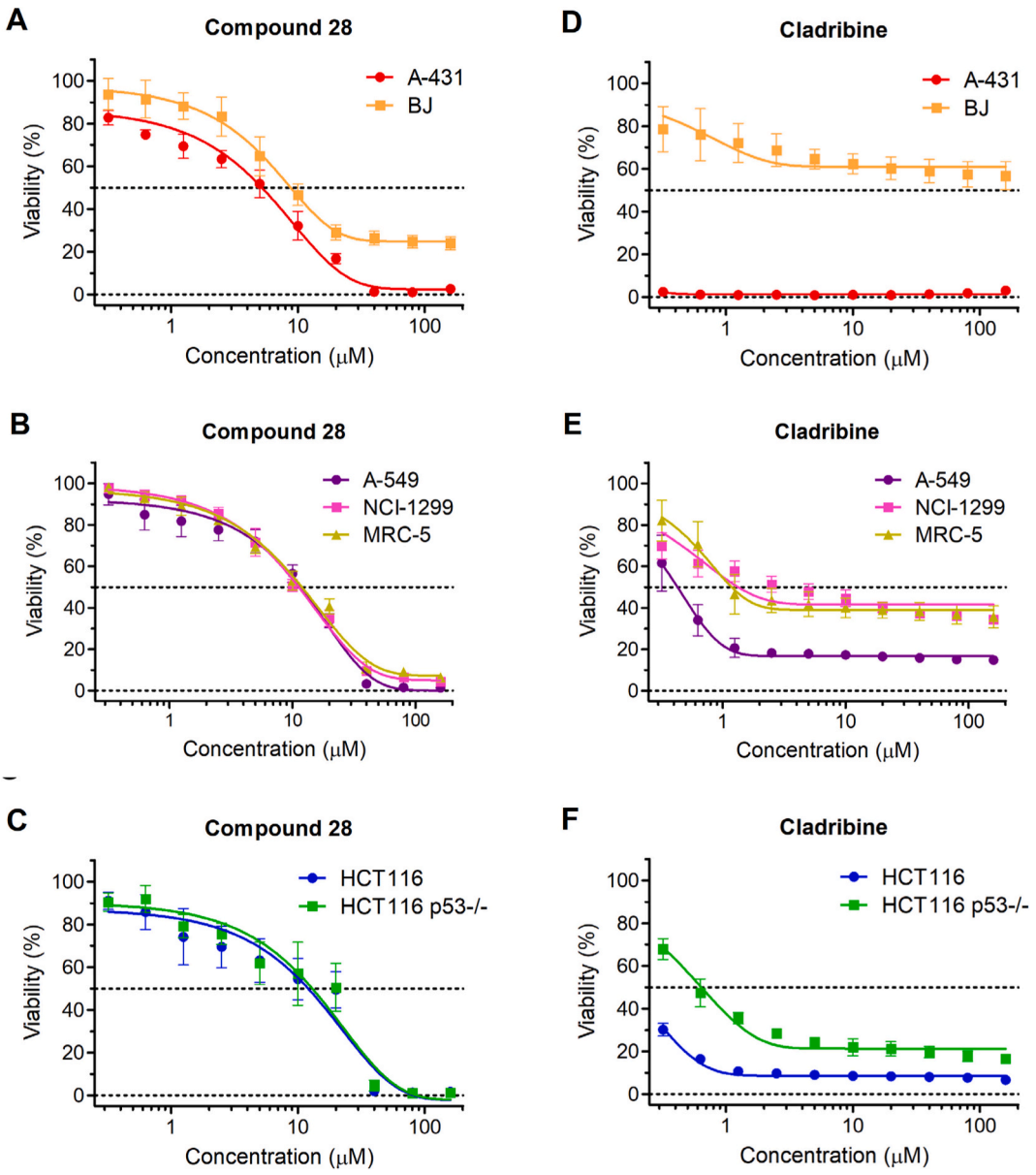

Fig. 5. The viability of selected cancer and normal cell lines in response to compound **28** (A–C) and cladribine (D–F) assessed using the MTT assay. The cancer cell lines included epidermoid carcinoma A-431, lung carcinomas A-549 and NCI-H1299, and colorectal carcinomas HCT116 and HCT116 p53−/−. Normal cell lines included normal epidermoid fibroblasts BJ and normal lung fibroblasts MRC-5. Cells were treated with increasing concentrations of the indicated compounds (0.32–160 μM) for 72 h. Cell viability inhibition was calculated relative to untreated controls. Data points represent mean ± SD from at least four independent experiments.

limited selectivity, indicating that increased cytotoxicity does not necessarily translate into an improved therapeutic window. Interestingly, the structural determinants of potency did not fully overlap with those governing selectivity, suggesting that optimization of therapeutic selectivity will require structural refinement beyond simply maximizing cytotoxic activity.

3.4.3. SAR for antiviral activity

Antiviral activity followed a structure–activity relationship pattern clearly distinct from that observed for cytotoxic effects, indicating different pharmacophoric requirements for antiviral *versus* anticancer activity. Notably, the most active antiviral compounds were not the most cytotoxic derivatives, suggesting that antiviral efficacy was not merely a consequence of nonspecific host-cell toxicity.

The strongest inhibition of **HPIV-3** replication was observed for compounds **22**, **25**, and **35**; however, only compounds **22** and **35** displayed favorable selectivity, indicating genuine antiviral potential. These findings suggest that antiviral activity against **HPIV-3** depends on specific structural features of the N^6 substituent rather than simply increasing overall hydrophobicity or cytotoxic potency.

In contrast, activity against **AdV5** followed a different structural trend. The most active and selective anti-**AdV5** compound was **12**, bearing a polar *N*-methylpiperazine substituent, whereas the **HPIV-3**-active compounds possessed markedly different substitution patterns. This suggests that antiviral activity against distinct viral targets may require different physicochemical and structural properties.

Overall, the antiviral SAR appears more target-specific and less broadly predictable than the cytotoxic SAR, highlighting the need for further structural optimization to identify more selective antiviral leads.

3.5. Exposure to compound **28** inhibits proliferation and induces cell death independently of p53 status

The sensitivity of the HCT116 and HCT116 p53−/− cell lines to compound **28** was evaluated using the IncuCyte S3 Live-Cell Imaging System to monitor cell proliferation and cell death, including apoptosis, in p53-proficient and p53-deficient backgrounds. Cladribine was used as a reference anticancer drug. Cells were treated with compound **28** or CL at concentrations of 10 μM, 20 μM, and 40 μM, and images were acquired every 6 h over a period of 96 h (Figs. 6A–8A and Figs. S5–S7, S8A and S9, SI_1). Under untreated conditions, HCT116 and HCT116 p53−/− cells reached average confluence levels of 84% and 82%, respectively, by day 4 (Fig. 6B–E). Exposure to compound **28** resulted in a pronounced reduction in cell proliferation in both cell lines. Growth inhibition was dose-dependent and comparable between p53-proficient and p53-deficient cells. On day 4, confluence in HCT116 cells treated with **28** reached 40%, 36%, and 5%, while HCT116 p53−/− cells reached 40%, 33%, and 6% following treatment with 10 μM, 20 μM, and 40 μM, respectively (Fig. 6B–D). In contrast, the response to cladribine was dependent on p53 status. From day 2 onward, *TP53*-deleted cells exhibited significantly higher confluence than p53-proficient HCT 116 cells ($p < 0.05$), although growth inhibition by CL was not dose-dependent. By day 4, confluence values reached 7%, 6%, and 5% in HCT116 cells and 9%, 10%, and 9% in HCT116 p53−/− cells treated with 10 μM, 20 μM, and 40 μM CL, respectively (Figs. 6B, C, and E).

To provide a more quantitative assessment of the antiproliferative effects of compound **28** and cladribine, the specific growth rate (μ, h^{-1}) was calculated for each experimental condition based on the exponential phase of the growth curves obtained from IncuCyte live-cell imaging (Fig. 6B and C). Under untreated conditions, HCT116 and HCT116 p53−/− cells exhibited comparable baseline growth rates, indicating similar intrinsic proliferative capacity irrespective of p53 status. Treatment with compound **28** resulted in a concentration-dependent decrease in μ values in both cell lines ($p < 0.005$; SI_2). Importantly, the magnitude of growth-rate inhibition was similar, or slightly more pronounced, in HCT116 compared with HCT116 p53−/− cells across all tested concentrations, indicating that the antiproliferative activity of compound **28** is largely independent of p53. In contrast, cladribine treatment led to a significantly greater reduction in μ values in p53-proficient HCT116 cells than in p53-deficient HCT116 cells ($p < 0.05$; SI_2). Collectively, the quantitative growth-rate analysis demonstrates that compound **28** suppresses cell proliferation with comparable efficiency in p53-proficient and p53-deficient colorectal carcinoma cells, whereas the antiproliferative activity of cladribine is strongly influenced by p53 status.

The effects of compound **28** and CL on cell viability were further evaluated using the SYTOX Green Dead Cell Stain, which labels dead cells independently of the mode of cell death (Fig. 7 and Fig. S6, SI_1). No significant increase in cell death was observed in untreated cells or in cells treated with compound **28** at concentrations of 10 or 20 μM in HCT116 cells, or at 10 μM in HCT116 p53−/− cells ($p > 0.05$). In contrast, exposure to 40 μM of compound **28** resulted in a significant increase in cell death ($p < 0.001$), which reached a plateau after approximately 72 h (Fig. 7B and C and SI_2). The rate of cell death between days 1 and 4 was comparable or slightly higher in HCT116 cells than in HCT116 p53−/− cells; however, p53-deficient cells exhibited a higher baseline number of dead cells at the beginning of the experiment (Fig. 7D and SI_2). In the case of CL, the kinetics of cell death differed markedly between p53-proficient and p53-deficient cells (Fig. 7B, C, and E and SI_2). In HCT116 cells, a significant increase in SYTOX Green-positive cells was detected as early as 36 h after treatment (Fig. 7B). In contrast, HCT116 p53−/− cells displayed a much flatter death curve, with a delayed increase observed only after 48 h, indicating reduced cell death dynamics in the absence of p53 (Fig. 7C). Accordingly, the level of cell death at 96 h was significantly lower in HCT116 p53−/− cells than in HCT116 cells (0.34, 0.34, and 0.37 relative units *vs* 0.47, 0.44, and 0.43 relative units, respectively; $p < 0.01$; Fig. 7B–E). Importantly, the overall cell death curves in both cell lines followed a similar pattern across **28** and CL concentrations.

To identify the mode of cell death induced by compound **28** and CL, apoptosis was assessed using an Annexin V antibody conjugated to Alexa Fluor 594, which enables rapid and reliable detection of early apoptotic events. Our findings demonstrated that both **28** and CL induced apoptosis in the tested cell lines (Fig. 8 and Fig. S7, SI_1 and SI_2). The kinetics of apoptosis closely matched the death rates measured using the SYTOX Green Dead Cell Stain. A substantial number of apoptotic cells was detected in untreated samples, and this number increased significantly following treatment with 40 μM compound 28 ($p < 0.001$, Fig. 8D and SI_2). In p53-deficient cells, however, apoptosis was also observed at a lower concentration of the compound (Fig. 8D). Taking into account the higher initial number of non-viable cells, no significant differences in overall apoptosis rates were observed between HCT116 and HCT116 p53−/− cells overall (SI_2). Nevertheless, a significantly higher proportion of apoptotic cells was detected in the p53−/− line after treatment with 10 μM **28** for 2–3 days and with 20 μM **28** for 1–3 days ($p < 0.05$; Fig. D). In contrast, the apoptotic response to CL differed between p53-proficient and p53-deficient cell lines. In both cell types, apoptosis was initiated later than in cells treated with compound **28**, becoming apparent only after 24 h, and no concentration-dependent differences were observed (Fig. 8B, C, E, and SI_2). Moreover, from the second day onward, significantly fewer p53-deficient cells underwent apoptosis compared with p53-proficient cells (Fig. 8E and SI_2). Analysis of the combined apoptotic and dead cell populations, identified by dual positivity for SYTOX Green and Annexin V, revealed that p53-deficient cells displayed a similar or slightly higher proportion of double-positive cells following treatment with compound **28**, but a significantly lower proportion after CL treatment (Figs. S8 and S9, SI_1 and SI_2).

In summary, compound **28** effectively inhibited cell proliferation and induced cell death in both p53-proficient HCT116 and p53-deficient HCT116 p53−/− colorectal carcinoma cells. Its antiproliferative activity was dose-dependent and comparable between the two cell lines, as demonstrated by confluence measurements and quantitative growth rate analyses, indicating that the activity of compound **28** is independent of p53 status. At higher concentrations, **28** induced significant cell death, predominantly through apoptosis, with similar overall kinetics in both cell lines. In contrast, the anticancer activity of cladribine was strongly influenced by p53 status, with reduced growth inhibition, delayed cell death, and attenuated apoptotic responses observed in p53-deficient cells. The results are consistent with the existing literature, which shows that CL-induced cell death occurs through apoptosis and depends on the presence of functional p53 [41]. The ability of p53 to induce apoptosis in response to environmental or oncogenic stress is a key mechanism underlying its role as a tumor suppressor [42]. Given that the *TP53* tumor suppressor gene is inactivated more frequently than any other gene in human cancers, our findings may provide a foundation for developing more selective and less toxic chemotherapeutic agents.

3.6. Changes in cell morphology

The effects of compound **28** and CL on cell morphology were monitored using the IncuCyte S3 Live-Cell Imaging System. Representative images are shown in Fig. 9. A comparison between HCT116 and HCT116 p53−/− cells revealed no apparent differences in the morphological response to treatment, indicating that the observed effects were independent of p53 status. Notably, even at the lowest tested concentration (10 μM), clear morphological differences were observed between cells exposed to **28** and those treated with CL. Compound **28** markedly suppressed cell proliferation and, at higher concentration (40 μM), induced cell death. In contrast, CL not only reduced proliferation but also caused a pronounced increase in cell size, accompanied by nuclear enlargement and multinucleation. These features are consistent with the development of a senescence-like phenotype [18,19]. Such

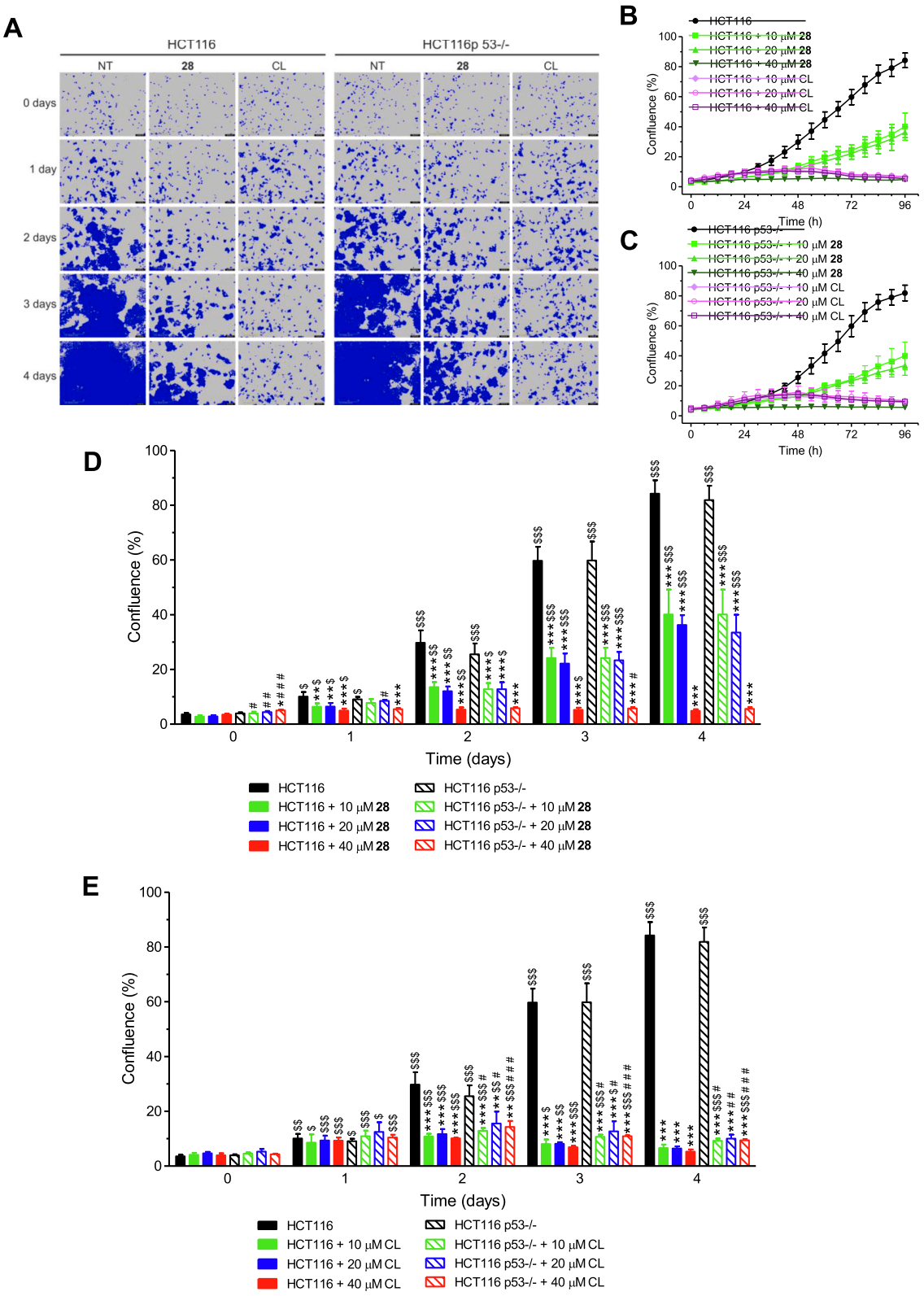

Fig. 6. Cell proliferation measured using the IncuCyte live-cell imaging in HCT116 and HCT116 p53−/− cells treated with 20 μM compound **28** or cladribine (CL) for up to 4 days. (A) Representative images show cell confluence (blue mask) captured on days 0, 1, 2, and 4 following treatment. NT, no treatment (DMSO control). Yellow scale bars in the lower-left corner of the images represent 400 μm. (B, C) Confluence of HCT116 cells and HCT116 p53−/−, respectively, expressed as a percentage of the total cell population. (D, E) Quantification of the confluence following treatment with **28** (upper graph) or CL (lower graph) at days 1–4. Data are presented as mean ± SD from four replicative wells. Statistical analysis was performed using one-way ANOVA followed by the Tukey's post-hoc test (*, $p < 0.05$; **, $p < 0.01$; ***, $p < 0.001$, treated cells *vs.* corresponding untreated cells at the same time point; $, $p < 0.05$; $$, $p < 0.01$; $$$, $p < 0.001$, treated cells *vs.* corresponding untreated cells at time 0 h) or two-tailed Student's *t*-test (#, $p < 0.05$; # #, $p < 0.01$; # # #, $p < 0.001$ HCT116 p53−/− cells *vs.* corresponding HCT116 cells). (For interpretation of the references to colour in this figure legend, the reader is referred to the web version of this article.)

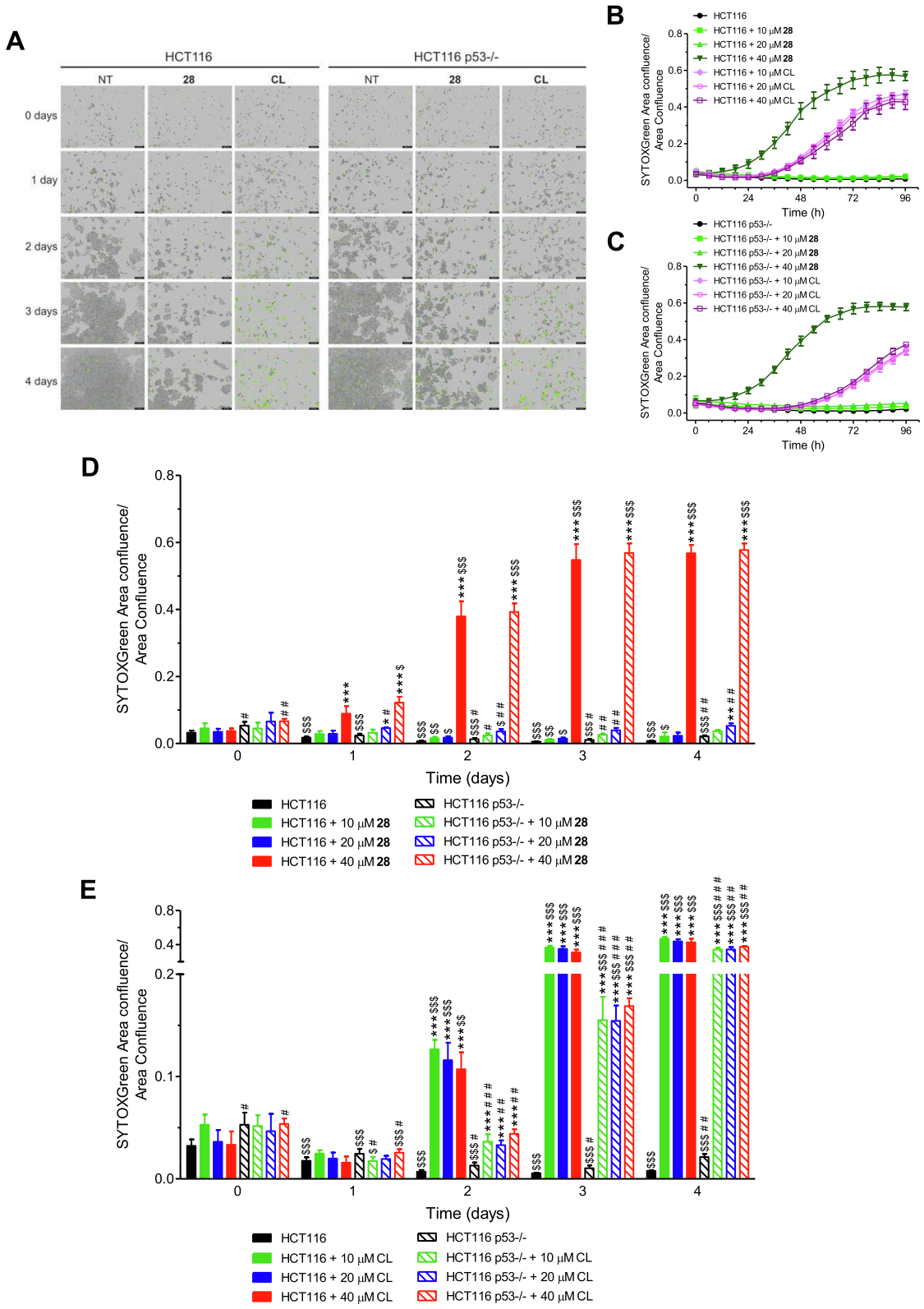

Fig. 7. Cell death measured using the IncuCyte live-cell imaging with SYTOXGreen Dead Cell Stain in HCT116 and HCT116 p53−/− cells treated with 20 μM compound **28** or cladribine (CL) for up to 4 days. (A) Representative images captured on days 0, 1, 2, and 4 following treatment. The green mask indicates dead cells. NT, no treatment (DMSO control). Yellow scale bars in the lower-left corner of the images represent 400 μm. (B, C) Cell death of HCT116 cells and HCT116 p53−/−, respectively, expressed as a percentage of the total cell population. (D, E) Quantification of cell death following treatment with **28** (upper graph) or CL (lower graph) at days 1–4. Data are presented as mean ± SD from four replicative wells. Statistical analysis was performed using one-way ANOVA followed by the Tukey's post-hoc test (*, $p < 0.05$; **, $p < 0.01$; ***, $p < 0.001$, treated cells *vs.* corresponding untreated cells at the same time point; $, $p < 0.05$; $$, $p < 0.01$; $$$, $p < 0.001$, treated cells *vs.* corresponding untreated cells at time 0 h) or two-tailed Student's *t*-test (#, $p < 0.05$; # #, $p < 0.01$; # # #, $p < 0.001$, HCT116 p53−/− cells *vs.* corresponding HCT116 cells). (For interpretation of the references to colour in this figure legend, the reader is referred to the web version of this article.)

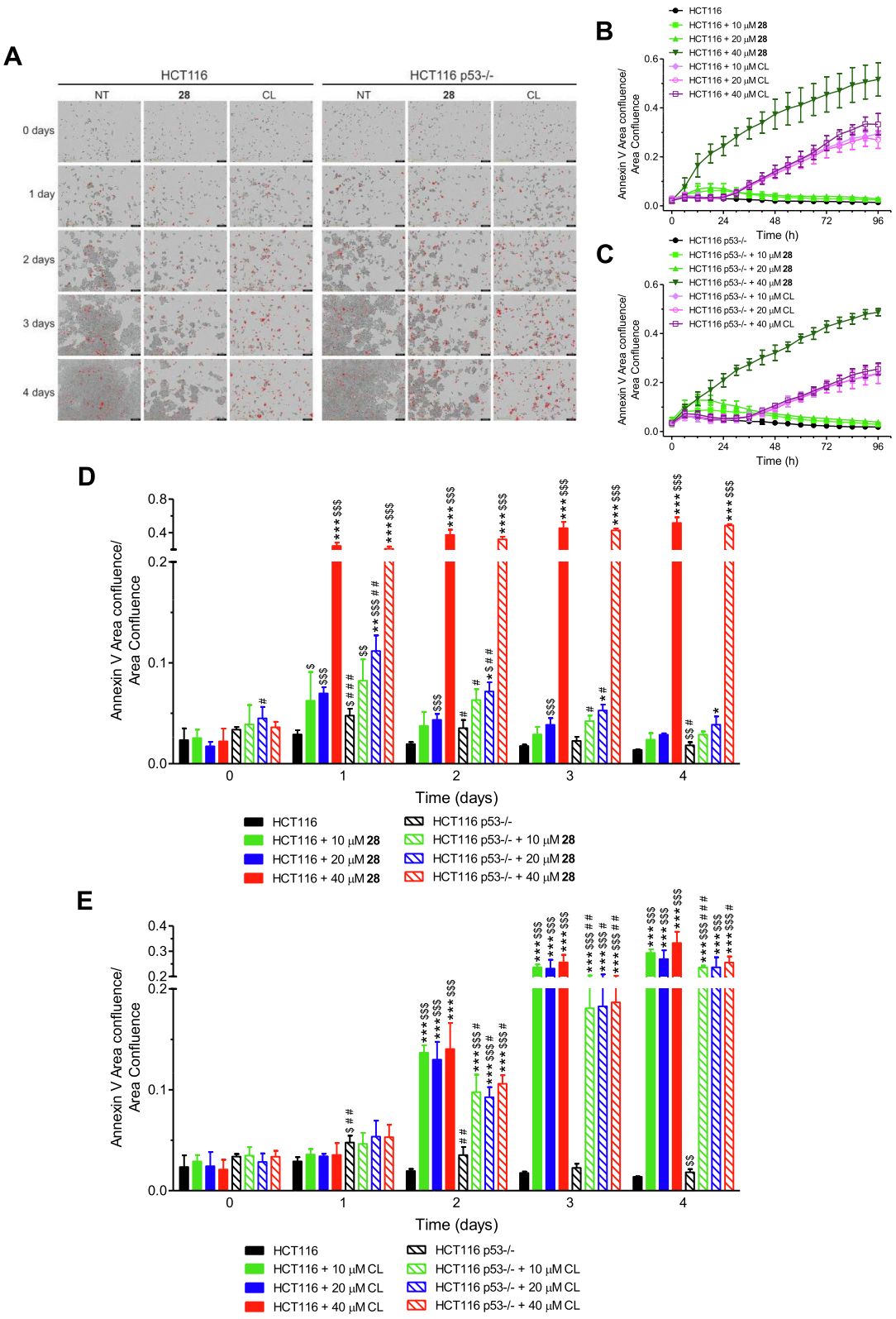

Fig. 8. Apoptosis assessed using the IncuCyte live-cell imaging with an anti-Annexin V antibody conjugated to Alexa Fluor 594 in HCT116 and HCT116 p53−/− cells treated with 20 μM compound **28** or cladribine (CL) for a period of up to 4 days. (A) Representative images captured on days 0, 1, 2, and 4 following treatment. The red mask indicates apoptotic cells. NT, no treatment (DMSO control). Yellow scale bars in the lower-left corner of the images represent 400 μm. (B, C) Apoptosis of HCT116 cells and HCT116 p53−/− cells, respectively, expressed as a percentage of the total cell population. (D, E) Quantification of apoptosis following treatment with **28** (upper graph) or CL (lower graph) at days 1–4. Data are presented as mean ± SD from four replicative wells. Statistical analysis was performed using one-way ANOVA followed by the Tukey's post-hoc test (*, $p < 0.05$; **, $p < 0.01$; ***, $p < 0.001$, treated cells *vs.* corresponding untreated cells at the same time point; $, $p < 0.05$; $$, $p < 0.01$; $$$, $p < 0.001$, treated cells *vs.* corresponding untreated cells at time 0 h) or two-tailed Student's *t*-test (#, $p < 0.05$; # #, $p < 0.01$; # # #, $p < 0.001$, HCT116 p53−/− cells *vs.* corresponding HCT116 cells). (For interpretation of the references to colour in this figure legend, the reader is referred to the web version of this article.)

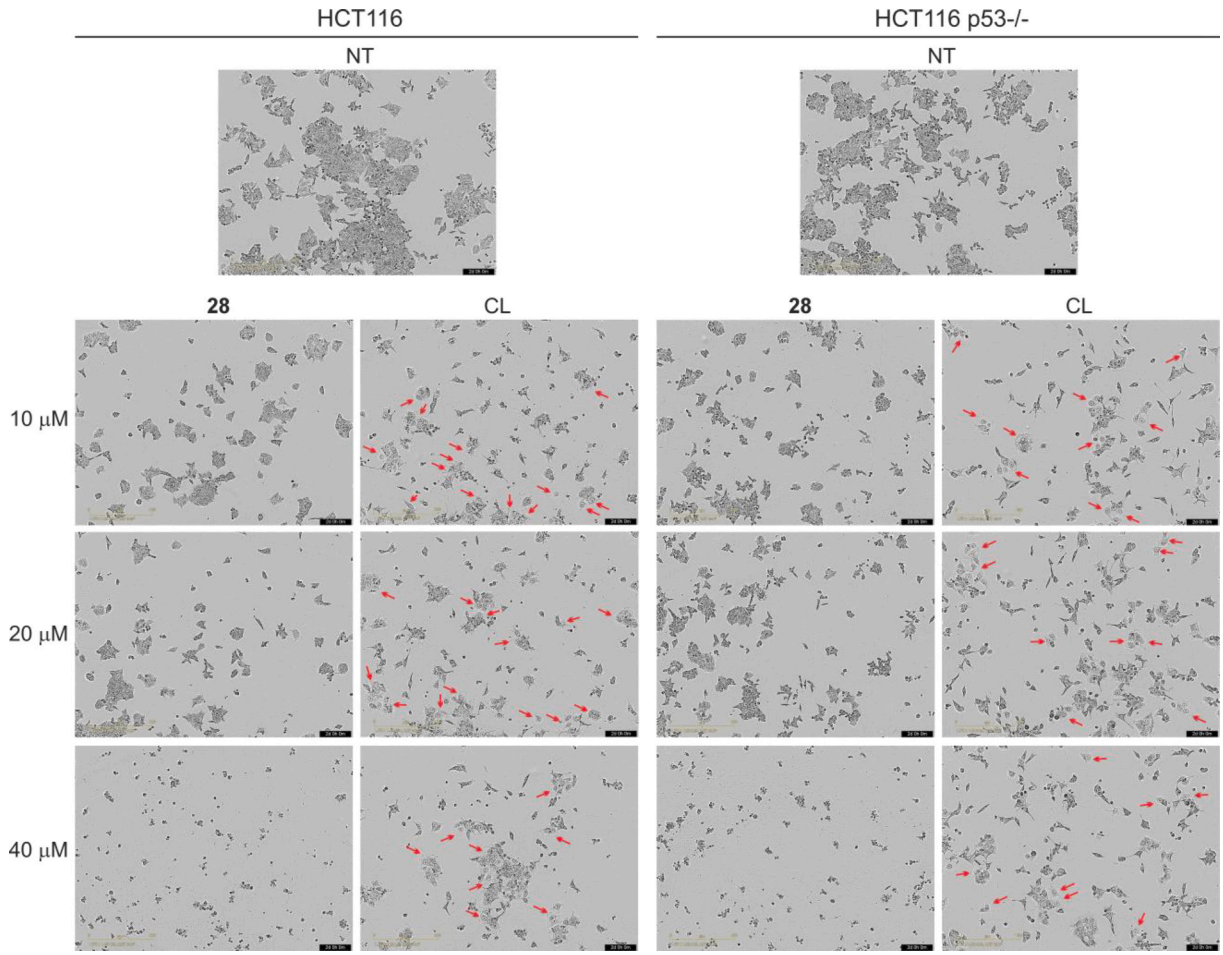

Fig. 9. Morphological changes in HCT116 and HCT116 p53−/− cells following 48 h exposure to compound **28** or cladribine (CL) at 10 μM, 20 μM, or 40 μM, visualized using the IncuCyte live-cell imaging System. Representative images show mononuclear and multinuclear cell morphologies. Red arrows indicate giant cells. NT, no treatment (DMSO control). (For interpretation of the references to colour in this figure legend, the reader is referred to the web version of this article.)

morphological alterations, including cellular hypertrophy and multinucleation, are hallmark characteristics of cellular senescence and are typically associated with irreversible cell-cycle arrest rather than acute cytotoxicity [43,44]. Consistently, after 48 h of incubation with compound **28** at 40 μM, cells of both cell lines were completely non-viable, whereas CL-treated cells remained largely viable (Fig. 9).

*3.7. Compound **28** interferes with cell cycle progression, regardless of p53 status*

To investigate whether compound **28** affects cell cycle progression, we quantitatively analyzed the distribution of cells across the G1, S, and G2/M phases at defined time points during treatment. Fig. 10 illustrates the changes in the cell cycle profiles of HCT116 and HCT116 p53−/− cells exposed to compound **28** (20 μM). In untreated samples, p53-deficient cells showed a higher proportion in S phase and a lower proportion in G1 than p53-proficient cells. Following exposure to **28**, both cell lines exhibited a time-dependent accumulation of cells in the G2/M phase, accompanied by a decrease in the G1 fraction. This pattern persisted for up to 9 h. From 12 h onward, the proportion of cells in G2/M declined, while the G1 population increased markedly. After 24 h of treatment, only approximately 5% of HCT116 cells and 9% of HCT116 p53−/− cells remained in S phase (undergoing DNA replication). Importantly, the overall cell cycle progression profile was nearly identical in both cell lines treated with compound **28**, indicating that interference with cell-cycle progression occurs independently of p53 status.

Overall, compound **28** induced pronounced morphological alterations in colorectal carcinoma cells that were distinct from those caused by cladribine and were independent of p53 status. While CL treatment led to an increase in cell size, nuclear enlargement, and the appearance of multinucleated cells, features consistent with a senescence-like phenotype, compound **28** primarily suppressed cell proliferation and, at higher concentrations, rapidly induced loss of cell viability. These morphological changes correlated with a complete loss of viable cells after 48 h of treatment with 40 μM compound **28**, in contrast to the largely viable, senescent-like cells observed following CL exposure. Consistent with these observations, **28** markedly interfered with cell-cycle progression in both p53-proficient and p53-deficient cells. Treatment resulted in a transient accumulation of cells in the G2/M phase, followed by a pronounced depletion of S-phase cells and a subsequent increase in the G1 population. The nearly identical cell-cycle profiles observed in HCT116 and HCT116 p53−/− cells demonstrated that the cell-cycle–modulating effects of compound **28** occur independently of p53 status. Together, these findings indicate that **28** disrupts tumor cell proliferation through p53-independent mechanisms involving both cell-cycle arrest and induction of cell death, distinguishing its mode of action from that of cladribine.

4. Summary and conclusions

In this study, a library of various N^6-modified adenosine derivatives (**7**–**36**) was synthesized in a single step and thoroughly characterized, including X-ray structures for selected compounds. Importantly, the

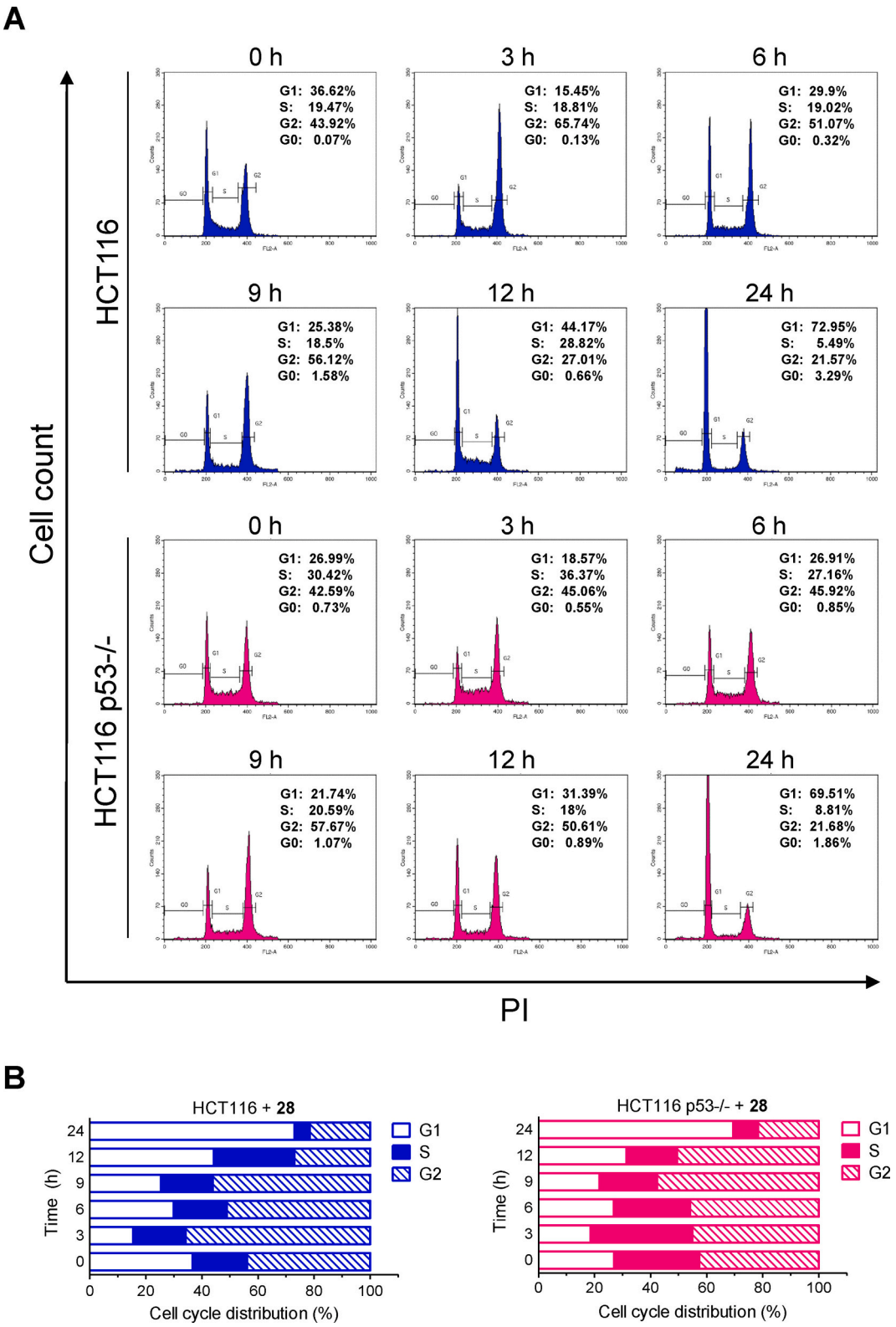

Fig. 10. Cell cycle analysis by flow cytometry in HCT116 cells and HCT116 p53−/− cells following exposure to compound **28**. (A) Representative histograms showing DNA content in untreated cells and cells treated with compound **28** (40 μM) for 3, 6, 12, and 24 h. PI, propidium iodide; G0, subG1. (B) Quantification of cell cycle distribution at each time point, illustrating the percentage of cells in the G1, S, and G2/M phases after treatment with compound **28** (40 μM).

library comprised both new and previously reported N^6-substituted adenosines; however, their anticancer and antiviral activities were evaluated systematically for the first time. Despite structural differences, the derivatives exhibited similar intramolecular hydrogen-bonding patterns and ribose conformations. Cytotoxicity was assessed across a broad panel of human cancer and normal cell lines, including p53-proficient and p53-deficient colorectal carcinoma cell lines. Among the tested compounds, **28** exhibited the highest potency, inhibiting

proliferation and inducing apoptosis regardless of p53 status, in contrast to cladribine, whose activity was strongly influenced by p53. Structure–activity relationship analysis revealed that the biological properties of N^6-modified adenosines are strongly governed by the nature of the N^6 substituent, with distinct structural requirements for cytotoxic, antiviral, and p53-independent activities. Live-cell imaging, together with SYTOX Green/Annexin V assays, confirmed a dose-dependent induction of apoptosis by compound **28**, while cell cycle analysis revealed G2/M arrest, followed by G1 accumulation. In contrast to the senescence-like phenotype induced by cladribine, compound **28** triggered rapid cell death. Antiviral screening identified compounds **22**, **25**, and **35** as potent inhibitors of human parainfluenza virus type 3, while compound **12** showed the highest activity and selectivity against human adenovirus type 5. However, for most derivatives, antiviral effects were observed at concentrations near the host-cell cytotoxicity threshold, thereby limiting their therapeutic potential. Importantly, only a limited subset of compounds (**9**, **12**, **16**, **22**, **23**, and **35**) exhibited favorable selectivity indexes against **HPIV-3** and/or **AdV5**, identifying these derivatives as preliminary scaffolds for further antiviral optimization rather than fully developed antiviral leads. Overall, the present study identified N^6-modified adenosines as a promising class of compounds for the further development of anticancer agents with p53-independent activity and highlights selected derivatives as attractive starting points for the rational design of more selective antiviral agents targeting respiratory pathogens. Future studies will focus on identifying the direct molecular targets of compound **28**, elucidating the molecular mechanisms underlying its anticancer and antiviral activities, and defining the mode of antiviral action of the most promising antiviral derivatives.

CRediT authorship contribution statement

Elżbieta Speina: Writing – review & editing, Writing – original draft, Visualization, Validation, Methodology, Investigation, Formal analysis, Data curation, Conceptualization. **Katherine Burchiellaro:** Investigation. **Marta Denel-Bobrowska:** Investigation. **Marta K. Dudek:** Investigation, Data curation. **Damian Trzybiński:** Writing – original draft, Visualization, Investigation, Formal analysis, Data curation. **Krzysztof Woźniak:** Investigation, Formal analysis. **Agnieszka B. Olejniczak:** Writing – original draft, Visualization, Investigation, Formal analysis, Data curation. **Adam Mieczkowski:** Writing – review & editing, Writing – original draft, Visualization, Validation, Supervision, Methodology, Investigation, Funding acquisition, Formal analysis, Data curation, Conceptualization.

Funding

This study was supported by the Institute of Biochemistry and Biophysics PAS (internal grant number FBW-MG-02/2023).

Declaration of competing interest

The authors declare that they have no known competing financial interests or personal relationships that could have appeared to influence the work reported in this paper.

Acknowledgments

Agnieszka B. Olejniczak and **Marta Denel-Bobrowska** thank the Polish Ministry of Science and Higher Education for financial support under the POL-OPENSCREEN project, decision no. 2024/WK/06. The X-Ray diffractometric measurements were performed at the Core Facility for Crystallographic and Biophysical Research to support the development of medicinal products sponsored by the Fundation for Polish Science (FNP). Upgrade of the Avance III 500 NMR spectrometer used to obtain results included in this publication was supported by the funds from the EU Regional Operational Program of the Lodz Region, RPLD.01.01.00-10-0008/18.

Appendix A. Supplementary data

Supplementary data to this article can be found online at https://doi.org/10.1016/j.bioorg.2026.110335.

Data availability

Data will be made available on request. The CCDC 2512665-2512667 contain supplementary crystallographic data for this paper. The data can be obtained free of charge from the Cambridge Crystallographic Data Centre *via* www.ccdc.cam.ac.uk/structures.

References

[1] K.L. Seley-Radtke, M.K. Yates, The evolution of nucleoside analogue antivirals: a review for chemists and non-chemists. Part 1: early structural modifications to the nucleoside scaffold, Antivir. Res. 154 (2018) 66–86, https://doi.org/10.1016/j.antiviral.2018.04.004.
[2] M.K. Yates, K.L. Seley-Radtke, The evolution of antiviral nucleoside analogues: a review for chemists and non-chemists. Part II: complex modifications to the nucleoside scaffold, Antivir. Res. 162 (2019) 5–21, https://doi.org/10.1016/j.antiviral.2018.11.016.
[3] J. Shelton, X. Lu, J.A. Hollenbaugh, J.H. Cho, F. Amblard, R.F. Schinazi, Metabolism, biochemical actions, and chemical synthesis of anticancer nucleosides, nucleotides, and base analogs, Chem. Rev. 116 (2016) 14379–14455, https://doi.org/10.1021/acs.chemrev.6b00209.
[4] M. Guinan, C. Benckendorff, M. Smith, G.J. Miller, Recent advances in the chemical synthesis and evaluation of anticancer nucleoside analogues, Molecules 25 (2020) 2050, https://doi.org/10.3390/molecules25092050.
[5] L. Hruba, V. Das, M. Hajduch, P. Dzubak, Nucleoside-based anticancer drugs: mechanism of action and drug resistance, Biochem. Pharmacol. 215 (2023) 115741, https://doi.org/10.1016/j.bcp.2023.115741.
[6] M. Scrima, G. Lauro, M. Grimaldi, S. Di Marino, A. Tosco, P. Picardi, P. Gazzerro, R. Riccio, E. Novellino, M. Bifulco, G. Bifulco, A.M. D'Ursi, Structural evidence of N^6-isopentenyladenosine as a new ligand of farnesyl pyrophosphate synthase, J. Med. Chem. 57 (2014) 7798–7803, https://doi.org/10.1021/jm500869x.
[7] A. Dassano, M. Mancuso, P. Giardullo, L.D. Cecco, P. Ciuffreda, E. Santaniello, A. Saran, T.A. Dragani, F. Colombo, N6-isopentenyladenosine and analogs activate the NRF2-mediated antioxidant response, Redox Biol. 2 (2014) 580–589, https://doi.org/10.1016/j.redox.2014.03.001.
[8] R. Ottria, S. Casati, E. Baldoli, J.A.M. Maier, P. Ciuffreda, N^6-alkyladenosines: synthesis and evaluation of in vitro anticancer activity, Bioorg. Med. Chem. 18 (2010) 8396–8402, https://doi.org/10.1016/j.bmc.2010.09.030.
[9] R. Ranieri, E. Ciaglia, G. Amodio, P. Picardi, M.C. Proto, P. Gazzerro, C. Laezza, P. Remondelli, M. Bifulco, S. Pisanti, N^6-isopentenyladenosine dual targeting of AMPK and Rab7 prenylation inhibits melanoma growth through the impairment of autophagic flux, Cell Death Differ. 25 (2018) 353–367, https://doi.org/10.1038/cdd.2017.165.
[10] M.F. Biabani, S.P. Gunasekera, R.E. Longley, A.E. Wright, S.A. Pomponi, Tubercidin, a cytotoxic agent from the marine sponge *Caulospongia biflabellata*, Pharm. Biol. 40 (2002) 302–303, https://doi.org/10.1076/phbi.40.4.302.8469.
[11] E. Van Den Neste, S. Cardoen, F. Offner, F. Bontemps, Old and new insights into the mechanisms of action of two nucleoside analogs active in lymphoid malignancies: fludarabine and cladribine (review), Int. J. Oncol. 27 (2005) 1113–1124, https://doi.org/10.3892/ijo.27.4.1113.
[12] J. Chen, The cell-cycle arrest and apoptotic functions of p53 in tumor initiation and progression, Cold Spring Harb. Perspect. Med. 6 (2016) a026104, https://doi.org/10.1101/cshperspect.a026104.
[13] T. Ozaki, A. Nakagawara, Role of p53 in cell death and human cancers, Cancers 3 (2011) 994–1013, https://doi.org/10.3390/cancers3010994.
[14] D. Speidel, The role of DNA damage responses in p53 biology, Arch. Toxicol. 89 (2015) 501–517, https://doi.org/10.1007/s00204-015-1459-z.
[15] X. Zhou, Q. Hao, H. Lu, Mutant p53 in cancer therapy—the barrier or the path, J. Mol. Cell Biol. 11 (2019) 293–305, https://doi.org/10.1093/jmcb/mjy072.
[16] K. Hientz, A. Mohr, D. Bhakta-Guha, T. Efferth, The role of p53 in cancer drug resistance and targeted chemotherapy, Oncotarget 8 (2016) 8921–8946, https://doi.org/10.18632/oncotarget.13475.
[17] M. Zhang, G. Zhuang, X. Sun, Y. Shen, W. Wang, Q. Li, W. Di, TP53 mutation-mediated genomic instability induces the evolution of chemoresistance and recurrence in epithelial ovarian cancer, Diagn. Pathol. 12 (2017) 16, https://doi.org/10.1186/s13000-017-0605-8.
[18] J. Campisi, F. d'Adda di Fagagna, Cellular senescence: when bad things happen to good cells, Nat. Rev. Mol. Cell Biol. 8 (2007) 729–740, https://doi.org/10.1038/nrm2233.
[19] T. Kuilman, C. Michaloglou, W.J. Mooi, D.S. Peeper, The essence of senescence, Genes Dev. 24 (2010) 2463–2479, https://doi.org/10.1101/gad.1971610.
[20] B.G. Childs, M. Durik, D.J. Baker, J.M. van Deursen, Cellular senescence in aging and age-related disease: from mechanisms to therapy, Nat. Med. 21 (2015) 1424–1435, https://doi.org/10.1038/nm.4000.

[21] M. Synowitz, R. Glass, K. Färber, D. Markovic, G. Kronenberg, K. Herrmann, J. Schnermann, C. Nolte, N. van Rooijen, J. Kiwit, H. Kettenmann, A1 adenosine receptors in microglia control glioblastoma-host interaction, Cancer Res. 66 (2006) 8550–8557, https://doi.org/10.1158/0008-5472.CAN-06-0365.
[22] A. Mieczkowski, M. Bazlekowa, M. Bagiński, J. Wójcik, A. Winczura, A. Miazga, S. Shahmoradi Ghahe, R. Gajda, K. Woźniak, B. Tudek, A mild and efficient approach to the 6*H*-oxazolo[3,2-*f*]pyrimidine-5,7-dione scaffold via unexpected rearrangement of 2,3-dihydropyrimido[6,1-*b*][1,5,3]dioxazepine-7,9(5*H*,8*H*)-diones: synthesis, crystallographic studies, and cytotoxic activity screening, Tetrahedron Lett. 57 (2016) 743–746, https://doi.org/10.1016/j.tetlet.2016.01.006.
[23] A. Mieczkowski, P. Wińska, M. Kaczmarek, M. Mroczkowska, D. Garbicz, T. Pilżys, M. Marcinkowski, J. Piwowarski, E. Grzesiuk, 2′-Deoxy-2′-azidonucleoside analogs: synthesis and evaluation of antitumor and antimicrobial activity, Chem. Pap. 72 (2018) 981–990, https://doi.org/10.1007/s11696-017-0339-9.
[24] A. Mieczkowski, M. Makowska, J. Sekula, E. Tomczyk, E. Zalewska, A. Nasulewicz-Goldeman, J. Wietrzyk, Bicyclic cytarabine analogues: synthesis and investigation of antitumor properties of novel, 6-aryl- and 6-alkyl-3*H*-pyrrolo[2,3-*d*]pyrimidin-2(7*H*)-one arabinosides, Tetrahedron 71 (2015) 8454–8461, https://doi.org/10.1016/j.tet.2015.09.015.
[25] A. Mieczkowski, E. Tomczyk, M. Makowska, A. Nasulewicz-Goldeman, R. Gajda, K. Woźniak, J. Wietrzyk, Synthesis and investigation of the antitumor properties of novel, bicyclic furopyrimidine, pyrrolopyrimidine and pyrimidopyridazine nucleoside analogues, Synthesis 48 (2016) 566–572, https://doi.org/10.1055/s-0035-1561277.
[26] J.D. Żołnierczyk, A.B. Olejniczak, A. Mieczkowski, J.Z. Błoński, Z.M. Kiliańska, T. Robak, Z.J. Leśnikowski, In vitro antileukemic activity of novel adenosine derivatives bearing boron cluster modification, Bioorg. Med. Chem. 24 (2016) 5076–5087, https://doi.org/10.1016/j.bmc.2016.08.028.
[27] A. Mieczkowski, A. Kierozalska, M. Białek-Pietras, T.M. Goszczyński, S. Janczak, A. B. Olejniczak, M. Studzińska, E. Paradowska, Z.J. Leśnikowski, Comparative study of inorganic, boron-rich cluster and organic, phenyl adenosine modifications: synthesis and properties, Future Med. Chem. 11 (2019) 1267–1284, https://doi.org/10.4155/fmc-2018-0517.
[28] K. Bednarska-Szczepaniak, A. Mieczkowski, A. Kierozalska, D. Pavlović Saftić, K. Głąbała, T. Przygodzki, L. Stańczyk, K. Karolczak, C. Watała, H. Rao, Z.-G. Gao, K.A. Jacobson, Z.J. Leśnikowski, Synthesis and evaluation of adenosine derivatives as A1, A2A, A2B and A3 adenosine receptor ligands containing boron clusters as phenyl isosteres and selective A3 agonists, Eur. J. Med. Chem. 223 (2021) 113607, https://doi.org/10.1016/j.ejmech.2021.113607.
[29] CrysAlis CCD and CrysAlis RED, Oxford Diffraction Ltd, Yarnton, Oxfordshire, England, 2008.
[30] R.C. Clark, J.S. Reid, The analytical calculation of absorption in multifaceted crystals, Acta Cryst. A 51 (1995) 887–897, https://doi.org/10.1107/S0108767395007367.
[31] A.L. Spek, Structure validation in chemical crystallography, Acta Cryst. D 65 (2009) 148–155, https://doi.org/10.1107/S090744490804362X.
[32] G.M. Sheldrick, Crystal structure refinement with SHELXL, Acta Cryst. C 71 (2015) 3–8, https://doi.org/10.1107/S2053229614024218.
[33] O.V. Dolomanov, L.J. Bourhis, R.J. Gildea, J.a.K. Howard, H. Puschmann, OLEX2: a complete structure solution, refinement and analysis program, J. Appl. Crystallogr. 42 (2009) 339–341, https://doi.org/10.1107/S0021889808042726.
[34] C.F. Macrae, I.J. Bruno, J.A. Chisholm, P.R. Edgington, P. McCabe, E. Pidcock, L. Rodriguez-Monge, R. Taylor, J. van de Streek, P.A. Wood, Mercury CSD 2.0 – new features for the visualization and investigation of crystal structures, J. Appl. Crystallogr. 41 (2008) 466–470, https://doi.org/10.1107/S0021889807067908.
[35] Z.J. Leśnikowski, E. Paradowska, A.B. Olejniczak, M. Studzińska, P. Seekamp, U. Schüßler, D. Gabel, R.F. Schinazi, J. Plešek, Towards new boron carriers for boron neutron capture therapy: metallacarboranes and their nucleoside conjugates, Bioorg. Med. Chem. 13 (2005) 4168–4175, https://doi.org/10.1016/j.bmc.2005.04.042.
[36] A.B. Olejniczak, A.M. Adamska, E. Paradowska, M. Studzinska, P. Suski, Z. J. Leśnikowski, Modification of selected anti-HCMV drugs with lipophilic boron cluster modulator, Acta Pol. Pharm. 70 (2013) 489–504.
[37] G. Indrayanto, G.S. Putra, F. Suhud, Validation of *in-vitro* bioassay methods: application in herbal drug research, in: A.A.A. l-Majed (Ed.), Profiles of drug substances, excipients and related methodology, Academic Press, 2021, pp. 273–307, https://doi.org/10.1016/bs.podrm.2020.07.005.
[38] F. Steppeler, D. Iwan, R. Gaida, M. Denel-Bobrowska, A.B. Olejniczak, E. Wojaczyńska, Chiral 2-azabicycloalkanes bearing 1,2,3-triazole, thiourea, and ebselen moieties – synthesis and biological activity, Biomed. Pharmacother. 164 (2023) 114908, https://doi.org/10.1016/j.biopha.2023.114908.
[39] D. Hanahan, R.A. Weinberg, Hallmarks of Cancer: the next generation, Cell 144 (2011) 646–674, https://doi.org/10.1016/j.cell.2011.02.013.
[40] K.H. Vousden, D.P. Lane, p53 in health and disease, Nat. Rev. Mol. Cell Biol. 8 (2007) 275–283, https://doi.org/10.1038/nrm2147.
[41] E. Wawryk-Gawda, P. Chylińska-Wrzos, M. Lis-Sochocka, K. Chłapek, K. Bulak, M. Jędrych, B. Jodłowska-Jędrych, P53 protein in proliferation, repair and apoptosis of cells, Protoplasma 251 (2014) 525–533, https://doi.org/10.1007/s00709-013-0548-1.
[42] E.C. Pietsch, S.M. Sykes, S.B. McMahon, M.E. Murphy, The p53 family and programmed cell death, Oncogene 27 (2008) 6507–6521, https://doi.org/10.1038/onc.2008.315.
[43] J. Belhadj, S. Surina, M. Hengstschläger, A.J. Lomakin, Form follows function: nuclear morphology as a quantifiable predictor of cellular senescence, Aging Cell 22 (2023) e14012, https://doi.org/10.1111/acel.14012.
[44] M. Kloc, A. Uosef, A. Subuddhi, J.Z. Kubiak, R.P. Piprek, R.M. Ghobrial, Giant multinucleated cells in aging and senescence—an abridgement, Biology 11 (2022) 1121, https://doi.org/10.3390/biology11081121.